Published in final edited form as:
Cell Rep. 2020 November 24; 33(8): 108423. doi:10.1016/j.celrep.2020.108423.

Warburg-like Metabolic Reprogramming in Aging Intestinal Stem Cells Contributes to Tissue Hyperplasia

Otto Morris[1], **Hansong Deng**[2,3], **Christine Tam**[4], **Heinrich Jasper**[1,3,5,*]

[1]Immunology Discovery, Genentech, Inc., 1 DNA Way, South San Francisco, CA 94080, USA

[2]Shanghai East Hospital, School of Life Sciences and Technology, Tongji University, Shanghai 20092, China

[3]Buck Institute for Research on Aging, 8001 Redwood Boulevard, Novato, CA 94945-1400, USA

[4]Department of Biomolecular Resources, Genentech, Inc., 1 DNA Way, South San Francisco, CA 94080, USA

[5]Lead Contact

SUMMARY

In many tissues, stem cell (SC) proliferation is dynamically adjusted to regenerative needs. How SCs adapt their metabolism to meet the demands of proliferation and how changes in such adaptive mechanisms contribute to age-related dysfunction remain poorly understood. Here, we identify mitochondrial Ca^{2+} uptake as a central coordinator of SC metabolism. Live imaging of genetically encoded metabolite sensors in intestinal SCs (ISCs) of *Drosophila* reveals that mitochondrial Ca^{2+} uptake transiently adapts electron transport chain flux to match energetic demand upon proliferative activation. This tight metabolic adaptation is lost in ISCs of old flies, as declines in mitochondrial Ca^{2+} uptake promote a "Warburg-like" metabolic reprogramming toward aerobic glycolysis. This switch mimics metabolic reprogramming by the oncogene Ras^{V12} and enhances ISC hyperplasia. Our data identify a critical mechanism for metabolic adaptation of tissue SCs and reveal how its decline sets aging SCs on a metabolic trajectory reminiscent of that seen upon oncogenic transformation.

Graphical Abstract

---

[*]Correspondence: jasperh@gene.com.

AUTHOR CONTRIBUTIONS
O.M., H.D., and H.J. designed all experiments. O.M. performed all experiments. H.D. performed preliminary experiments. C.T. sub-cloned PercevalHR, Laconic and Mito-R-GECO1. O.M. and H.J. wrote the manuscript.

SUPPLEMENTAL INFORMATION
Supplemental Information can be found online at https://doi.org/10.1016/j.celrep.2020.108423.

DECLARATION OF INTERESTS
The authors declare no competing interests.

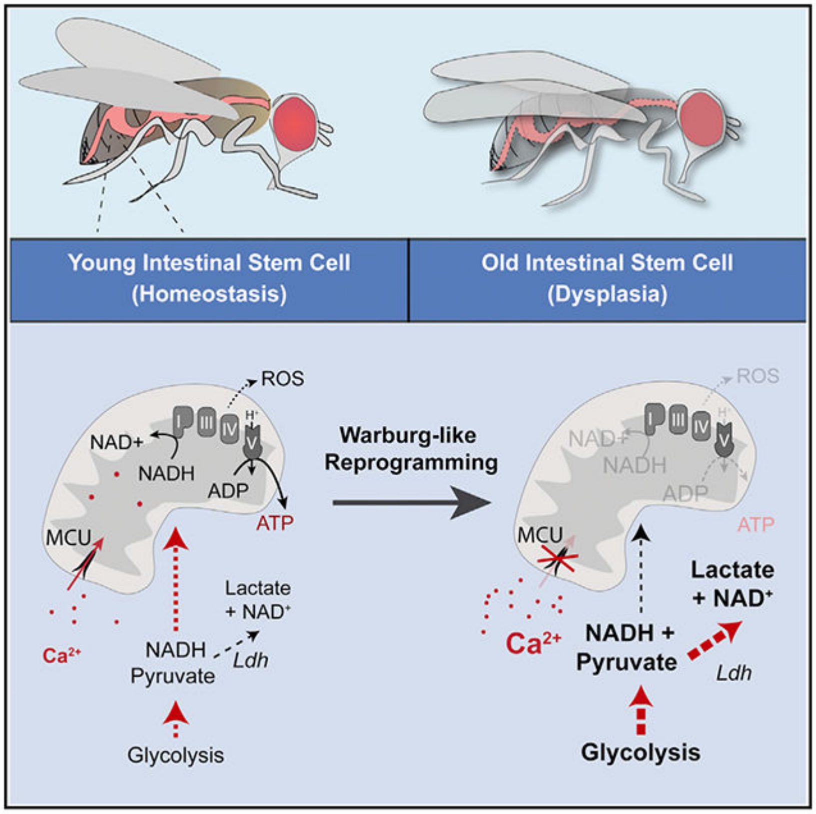

In Brief

Morris et al. uncover a Ca^{2+}-mediated adjustment of mitochondrial electron transport chain flux that links increased ATP production to proliferation in *Drosophila* intestinal stem cells. Declines in mitochondrial Ca^{2+} uptake in aging stem cells promote a Warburg-like metabolic reprogramming reminiscent of that observed upon oncogenic transformation.

INTRODUCTION

Somatic stem cells (SCs) maintain tissue homeostasis by tailoring their proliferative activity to the needs of the tissue. In barrier epithelia, SC activity is regulated by locally or systemically derived cytokines and growth factors, as well as by local mechanical stimuli (Deng et al., 2015; He et al., 2018; Miguel-Aliaga et al., 2018). These signals are integrated to orchestrate changes in cellular physiology required for efficient regeneration. Of central importance are metabolic changes (Chandel et al., 2016), which in response to the increased energetic and biosynthetic demands of SC division and differentiation, ensure optimal regenerative capacity. Although recent years have seen an explosion in our understanding of somatic SC regulation by mitogenic signals, little is known about how such signals achieve the required metabolic changes in SCs. It further remains unclear how aging and disease influence the metabolic adaptation of somatic SCs.

Metabolic alterations contribute to cancer and aging (Chandel et al., 2016; DeBerardinis and Chandel, 2016; Vander Heiden and DeBerardinis, 2017). A classic example is the “Warburg effect" or aerobic glycolysis, in which elevated glycolytic flux supports ATP demand but increases lactate generation and mitochondria pivot from pyruvate oxidation to supporting growth by enhanced lipid, nucleotide, and amino acid synthesis. These metabolic shifts support tumor initiation (Bensard et al., 2019), growth (Schell et al., 2014), and metastasis (Lu, 2019). Declines in mitochondrial respiratory activity also accompany aging of the human and murine brain, heart, and liver (Herbener, 1976; Ojaimi et al., 1999; Short et al., 2005; Yen et al., 1989) and were recently proposed as a biomarker of biological age (Ravera et al., 2019). Reversing these declines may have therapeutic benefit, as genetic and pharmacological treatments enhancing mitochondrial activity extend lifespan in multiple invertebrate models (Bahadorani et al., 2010; Hur et al., 2013; Palikaras et al., 2015; Rana et al., 2013; Rera et al., 2011; Sanz et al., 2010). Detailed *in vivo* characterization of metabolic changes in specific tissues and cell types in aging and disease is essential to gain further insight into their causes and consequences. Particularly pertinent are changes in SCs, whose metabolic demands vary greatly between episodes of quiescence and activity (Chandel et al., 2016) and whose aberrant function contributes to age-related declines in tissue homeostasis and cancer development (Chandel et al., 2016; DeBerardinis and Chandel, 2016). Here, we use *Drosophila* as a model system to investigate changes in mitochondrial function and metabolism in aging and oncogenic SCs.

The *Drosophila* intestinal epithelium has served as a productive model to elucidate mechanisms regulating intestinal SC (ISC) activity and function (Miguel-Aliaga et al., 2018). Although ISCs of young flies are mostly quiescent in homeostatic conditions, ISCs are activated in response to damage (Buchon et al., 2009b; Guo et al., 2014; Hochmuth et al., 2011; Jasper, 2020; Miguel-Aliaga et al., 2018). In a healthy regenerative response, such as that following bacterial infection in young flies, activated ISCs divide to replenish damage cells and restore homeostasis (Buchon et al., 2009b). These divisions are mostly asymmetric (Hu and Jasper, 2019), and in addition to another ISC, give rise to either an enterocyte-lineage-restricted diploid progenitor cell called an enteroblast (EB; approx. 90% frequency), or to an enteroendocrine cell (EE; approx. 10% frequency) (Miguel-Aliaga et al., 2018). However, in the aging intestine, commensal dysbiosis, chronic innate immune activation, and increased oxidative stress cause continual tissue damage, chronic ISC activity, and ISC mis-differentiation (Guo et al., 2014; Hochmuth et al., 2011; Jasper, 2020; Li et al., 2016). Whether these changes are associated with changes in the metabolic status of ISCs remains largely unclear, but it was shown that perturbations that promote mitochondrial biogenesis or that enhance electron transport chain (ETC) efficiency in ISCs can promote tissue homeostasis and extend lifespan (Hur et al., 2013; Rera et al., 2011).

Whether transient or chronic, in response to damage, ISCs are activated by a variety of mitogenic signals that trigger Jak/Stat, EGFR, and Wg signaling pathways (Miguel-Aliaga et al., 2018). These pathways converge to modulate cytosolic Ca^{2+} concentration (Cyto[Ca^{2+}])–a required step in ISC activation (Deng et al., 2015; He et al., 2018; Xu et al., 2017). This transition is likely to require changes in energy metabolism in ISCs, affording the possibility that increases in cellular [Ca^{2+}] are linked to changes in ISC metabolism.

To explore the link between mitogenic signals, [Ca^{2+}], and metabolic adaptation during ISC activation and to characterize age-related changes in this adaptation, we performed live imaging by using recently developed tools for *in vivo* detection of Ca^{2+} ions, reactive oxygen species (ROS), and metabolites in ISCs. We identify mitochondrial Ca^{2+} (Mito[Ca^{2+}]) as a central coordinator of metabolism in young ISCs and find that age-related declines in Mito[Ca^{2+}] uptake promote a "Warburg-like" metabolic reprogramming. This metabolic reprogramming is reminiscent of that observed during oncogenic transformation and contributes to age-dependent deregulation of SC function.

RESULTS

ATP/ADP Ratios Transiently Decrease during the Activation of Young ISCs but Are Chronically Low in Old ISCs

We hypothesized that the ATP/ADP ratios of young, quiescent; young, activated; and old chronically active ISCs might differ and thus inform upon underlying metabolic changes. To test this hypothesis, we generated transgenic flies in which the ATP/ADP sensor PercevalHR (Tantama et al., 2013) was expressed under the control of UAS. PercevalHR is a dual excitation/single emission sensor, whose excitation at 405 nm is enhanced by ADP binding and whose excitation at 488 nm is enhanced by ATP binding. Using *esg::Gal4*, we expressed PercevalHR in intestinal progenitor cells, which comprise ISCs and their daughter EBs, and live-imaged midguts *ex vivo* (Figure 1A; Hu and Jasper, 2019). Confirming the sensitivity of PercevalHR to metabolic perturbations, feeding flies respiratory inhibitors or knockdown of *levy*, a critical component of complex IV (CIV) of the ETC, lowered the ATP/ADP ratios of quiescent progenitor cells (Figures S1A and S1B).

Compared to young progenitor cells, old progenitor cells were energetically deficient and harbored significantly lower ATP/ADP ratios (Figures 1B and S1C). As for all age-dependent phenotypes presented throughout this study, comparable phenotypes were observed when we used either a shorter, 29°C aging model (Figure S1C) or a longer, 18°C aging model that in combination with the Gal4:Gal80ts system enabled the temporal modulation of genes in aged progenitor cells (Figure 1B). Comparable results were also obtained when analyzing the sensor intensity of individual cells across separate guts or when analyzing the average sensor intensity of all labeled cells per individual midgut image (Figures 1B and S1D). This was observed with all results presented within this study, and we chose to report data from individual cells throughout for consistency.

Because the ISCs of young, healthy midguts are largely quiescent, we hypothesized that the increased proliferative activity of old ISCs might underlie their lower ATP/ADP ratios. To test this, we examined the ATP/ADP ratios of young progenitor cells activated in response to infection with the mild enteropathogen *Erwinia carotovora carotovora 15* (*Ecc15*) (Buchon et al., 2009b; Deng et al., 2015). Following *Ecc15* infection, ISCs undergo transient activation (4 h–16 h post-infection [PI]), regenerate the epithelium, and return to quiescence (24 h–40 h PI) (Figures 1D and S1F; ISC activity was scored by quantifying phospho-histone-H3-positive, PH3+ cells per gut) (Buchon et al., 2009b; Deng et al., 2015). Consistent with a transient increase in energy consumption during ISC activation, ATP/ADP ratios decreased at the onset of ISC activity (4 h PI), stayed low during the peak period of ISC activity (8 h and 16 h PI), and recovered as ISCs approached a return to quiescence (24 h and 40 h PI; Figures 1C, 1D, and S1E). ATP consumption may, therefore, exceed production during ISC activation, whereas during the recovery phase, the ATP production rate must increase to restore the homeostatic ATP/ADP balance. This metabolic adaptation, which ensures energetic supply eventually catches up to demand, appears disrupted in old ISCs, whose aberrant proliferative activity correlates with chronically low energy status. To understand the origins of this dysfunction, we decided to explore the mechanism of this metabolic adaptation in young ISCs.

Young ISCs Uptake Ca^{2+} by MCU Complex, whereas Old ISCs Lack Efficient MCU Activity

The activation of ISCs during a regenerative response requires a rise in Cyto[Ca^{2+}] (Deng et al., 2015; He et al., 2018; Xu et al., 2017). In many cell types, Cyto[Ca^{2+}] is kept low by the concerted action of Ca^{2+} pumps and channels at the plasma membrane and intracellular stores like the endoplasmic reticulum (ER) and mitochondria (Giorgi et al., 2018). Mitochondria take up Ca^{2+} by the recently identified Mito[Ca^{2+}] Uniporter (MCU) (Baughman et al., 2011; De Stefani et al., 2011; Giorgi et al., 2018). Studies in mammalian heart and muscle have posited a role for changes in Mito[Ca^{2+}] in coupling ATP production to changes in energetic demand (Glancy and Balaban, 2012; Glancy et al., 2013; Kwong et al., 2015; Luongo et al., 2015); yet, a broader role for Mito[Ca^{2+}] in metabolic transitions has remained elusive. We hypothesized that upon activation of ISCs, increases in Cyto[Ca^{2+}] would result in increases in Mito[Ca^{2+}], potentially influencing mitochondrial metabolism.

To test this hypothesis, we explored the link between Mito [Ca^{2+}] and Cyto[Ca^{2+}] in young ISCs. We generated flies in which Mito[Ca^{2+}] could be live imaged in ISCs of intact midguts *ex vivo*. We expressed mitochondrially targeted Ca^{2+} sensors in progenitor cells or in ISCs only by combining esg::Gal4 with Su(H)::Gal80 to prevent expression in EBs (Wang et al., 2014). Live imaging of intestines of these flies revealed that mitochondria of young, quiescent ISCs exhibited short (12–24 s), frequent flashes of high Mito[Ca^{2+}] (Videos S1 and S2). These flashes were asynchronous between individual mitochondria, suggesting that individual mitochondria have distinct and restricted Ca^{2+} permeability rather than passively taking up Ca^{2+} from the cytosol. We hypothesized that the recently described MCU may be involved in this regulation.

The MCU complex is an evolutionarily conserved Ca^{2+} channel that functions as the primary route of Mito[Ca^{2+}] uptake in many cell types (Figure 2A; Giorgi et al., 2018). A multimeric integral membrane protein located within the inner mitochondrial membrane, the pore-forming MCU protein binds Ca^{2+} by a conserved DIME (or DXXE) motif (Baughman et al., 2011; Cao et al., 2017; De Stefani et al., 2011). Mutation of the DIME motif to QIMQ forms a dominant negative form of MCU (MCU^{DN}) that is incapable of Ca^{2+} transport (Baughman et al., 2011; Cao et al., 2017; Choi et al., 2017; De Stefani et al., 2011; Drago and Davis, 2016). Expression of MCU^{DN}, or knockdown of MCU in ISCs using two RNAi lines targeting different regions of the MCU gene, abolished Mito[Ca^{2+}] flashes and lowered Mito[Ca^{2+}] (Figures S2A and S2B). The recorded decreases in Ca^{2+} sensor intensity were a consequence of lower Mito[Ca^{2+}], as we recorded comparable results when the signal was normalized with mitochondrially targeted TdTomato (Figure 2B; Lee et al., 2018). In contrast, overexpressing functional versions of *Drosophila* MCU or human MCU (hMCU) in young, quiescent ISCs caused the normally asynchronous flashing of individual mitochondria to become synchronized (Videos S3 and S4), further suggesting that endogenous MCU function is limiting for Mito[Ca^{2+}] permeability.

To test a link between Cyto[Ca^{2+}] and Mito[Ca^{2+}] in ISCs, we knocked down Stim, an ER-resident protein required for store-operated Ca^{2+} entry (SOCE) (Deng et al., 2015, or the plasma membrane Ca^{2+} channel TrpA1 (Xu et al., 2017). Each knockdown lowered Mito[Ca^{2+}] (Figures 2C and 2D), while elevating Cyto[Ca^{2+}] by co-overexpression of Stim and its partner Ca^{2+} channel Orai (Deng et al., 2015), raised Mito[Ca^{2+}] (Figure 2E). Critically, Stim and Orai overexpression failed to raise Mito [Ca^{2+}] when accompanied by MCU knockdown, confirming that changes in Cyto[Ca^{2+}] are transmitted to Mito[Ca^{2+}] by the MCU complex (Figure 2E).

In some cell types, Mito[Ca^{2+}] uptake has been described to feedback on SOCE and, in turn, regulate the frequency of Cyto [Ca^{2+}] oscillations (Parekh, 2017). In young, quiescent ISCs, however, MCU knockdown did not detectably alter Cyto [Ca^{2+}] oscillation frequency, peak height, peak width, area under the curve (AUC), or average Cyto[Ca^{2+}]–as indicated by mean GCaMP3/mCherry ratios (Figure S2C). Therefore, Mito [Ca^{2+}] uptake does not reciprocally regulate cytosolic [Ca^{2+}] oscillations, placing Mito[Ca^{2+}] firmly downstream of Cyto [Ca^{2+}] in ISCs.

The mitochondria of young ISCs activated by an *Ecc15* infection lacked their characteristic Mito[Ca^{2+}] flashes (Video S5) and instead exhibited continuously high Mito[Ca^{2+}] levels, which is in line with the parallel rise in Cyto[Ca^{2+}] (Deng et al., 2015). Mito [Ca^{2+}] increased at the onset of ISC activation (4 h), remained high during the peak of ISC activity (8 h and 16 h), and decreased as ISCs returned to quiescence (40 h; Figure 2F). Knockdown of MCU or overexpression of MCU^{DN} in ISCs prevented this elevation in Mito[Ca^{2+}] (Figures 2G and 2H).

In stark contrast, Mito[Ca^{2+}] in old ISCs did not correlate with Cyto[Ca^{2+}]. Instead, despite age-dependent increases in Cyto [Ca^{2+}] (Deng et al., 2015), Mito[Ca^{2+}] was lower in old chronically active ISCs than in young, quiescent ISCs (Figure 2I) and was only slightly increased after *Ecc15* infection (Figures S2D and S2E).

We controlled for accuracy of our CEPIA3mt/MitoTdTomato setup by assessing maximal Mito[Ca^{2+}] recordings following ionomycin-induced mitochondrial membrane permeabilization across different experimental conditions and genotypes (Figures S2F and S2G), as well as by using an alternative Mito-R-GECO1/MitoGFP setup (Figure S2H).

Together, these data suggest efficient Mito[Ca^{2+}] uptake in young, but not old, ISCs.

Mito[Ca^{2+}] Uptake Supports the Proliferative Activity and ATP/ADP Ratios of Young ISCs

Because Mito[Ca^{2+}] increases after infection following a time course that precedes a restoration of ATP/ADP ratios and a return to quiescence, we hypothesized that Mito[Ca^{2+}] uptake modulates metabolism to support the energy demand of ISC proliferation. To test this hypothesis, we assessed the activity of MCU-deficient ISCs in young, unchallenged flies by lineage tracing them using mosaic analysis with a repressible cell marker (MARCM) (Lee and Luo, 2001). Clones generated from ISCs homozygous for a previously generated *MCU* null allele (*MCU*^{52}) were significantly smaller than those of wild-type ISCs, indicating a reduced proliferative activity of mutant cells (Figure 3A). *MCU*^{52} clones possessed a lower percentage of PDM1^{+} ECs and an increased percentage of Prosp^{-} PDM1^{-} cells with small nuclei (Figure 3A). These cells were likely ISCs and EBs, and consistent with this finding, *MCU*^{52} clones contained significantly more Delta^{+} ISCs per clone (Figure S3A). Knockdown of MCU or overexpression of MCU^{DN} also strongly suppressed the increase in ISC activity caused by *Ecc15* infection (Figures 3B, 3C, S3B, and S3C; ISC activity was scored by quantifying phospho-histone-H3-positive, PH3+ cells per gut; Buchon et al., 2009b; Deng et al., 2015). Decreases in ISC activity were not a consequence of any toxic effect of *MCU* loss-of-function upon ISCs, as similar short-term MCU^{DN} expression in young flies did not alter the percentage of Delta^{+} ISCs per midgut (Figure S3D). Together, these data suggest that in the absence of Mito[Ca^{2+}] uptake, ISCs have impaired proliferative activity and differentiate into ECs at a lower rate.

We next used our PercevalHR flies to examine whether Mito [Ca^{2+}] controls the energy status of young ISCs. MCU^{DN} expression lowered the ATP/ADP ratios of young, quiescent progenitor cells to those equal to active wild-type progenitor cells (Figure 3D). Moreover, unlike wild-type progenitor cells, ATP/ADP ratios of MCU^{DN}-expressing progenitor cells were refractory to *Ecc15* infection, remaining consistently low at 16 h PI (Figure 3D). These findings are consistent with the observed link between chronically low ATP/ADP ratios and low Mito[Ca^{2+}] in old ISCs (Figures 1B and 2I) and, thus, indicated that Mito[Ca^{2+}] is a central regulator of ISC energy status.

Mito[Ca^{2+}] Adjusts NADH Oxidation Rate to Maintain Metabolic Homeostasis of Young ISCs

Nicotinamide adenine dinucleotide (NADH) is an abundant redox cofactor that functions in multiple aspects of cellular metabolism (Stein and Imai, 2012). NADH produced by glycolysis and the tricarboxylic acid (TCA) cycle is oxidized by the ETC, resulting in efficient ATP production. Major pools of NADH/NAD+ reside in both mitochondrial and cytosolic compartments and are linked by the malate-aspartate shuttle (Davila et al., 2018). We asked whether Mito[Ca^{2+}] may impact NADH/NAD+ levels in ISCs during regeneration and generated transgenic flies expressing SoNaR (Zhao et al., 2015, 2016), a recently developed genetically encoded sensor that reports cytosolic NADH/NAD+ ratios. Similar to PercevalHR, SoNaR is a dual excitation/single emission sensor. Following sequential 405/488-nm excitation of SoNaR, comparative emission at 520 nm reveals a cell’s relative NADH/NAD+ ratio. When expressed in progenitor cells and using live imaging, SoNaR was acutely sensitive to genetic perturbations predicted to decrease NADH oxidation: disrupting the ETC or knocking down malate dehydrogenase, an essential component of the malate:aspartate shuttle (Gu et al., 2020; Lee et al., 2012), raised NADH/NAD+ ratios (Figures S3E and S3F). Crucially, cpYFP, the conventional fluorescent protein from which the modified SoNaR is derived, did not respond to perturbations altering SoNaR fluorescence (Figures S3G and S3H).

During ISC activation after *Ecc15* infection, SoNaR reported little difference between young, active, and quiescent progenitor cells (Figure 3E), suggesting that ISCs tightly control NADH production and oxidation to maintain optimal NADH/NAD+ ratios during activation. Overexpression of MCU^{DN}, on the other hand, sharply increased the NADH/NAD+ ratio of both young, quiescent and activated progenitor cells (Figures 3F, 3G, and 3H), suggesting that the uptake of Ca^{2+} into mitochondria is required to prevent NADH accumulation in both young, quiescent, and activated ISCs. This was somewhat unexpected, as mammalian studies report increases in both mitochondrial and cytosolic NADH/NAD+ ratios upon Mito[Ca^{2+}] uptake, through Ca^{2+}-dependent activation of matrix dehydrogenases such as pyruvate dehydrogenase (PDH), which generate NADH (Denton, 2009; Luongo et al., 2015; Marcu et al., 2014). We assessed the contribution of matrix dehydrogenases to NADH/NAD+ ratios in young ISCs by using two strategies: knockdown of the essential E1a subunit of PDH or knockdown of the mitochondrial pyruvate carrier 1 (MPC1)–the channel through which cytosolic pyruvate accesses the matrix (Bricker et al., 2012; Herzig et al., 2012; Schell et al., 2017) (RNAi lines for both PDH-E1a and MPC1 were previously validated; Colca et al., 2013; Mattila et al., 2018; Schell et al., 2017). Knockdown of PDH-E1a or MPC1 had little effect on the NADH/NAD+ ratios of young, quiescent (Figures S3I and S3J) and young, activated progenitor cells (Figure S3K). Moreover, PDH-E1a or MPC1 RNAi did not alter the elevated NADH/NAD+ ratios caused by MCU^{DN} co-expression (Figures S3I and S3J). Finally, using our ATP/ADP sensor, we found that knockdown of MPC1 failed to alter the ATP/ADP ratios of young, quiescent progenitor cells (Figure S3L). This was unlike disruption of the ETC, which lowered ATP/ADP ratios (Figure S3L). The effects of Mito[Ca^{2+}] on NADH/NAD+ and ATP/ADP ratios in young ISCs are thus likely elicited by a mechanism independent of matrix dehydrogenases (Figure 3I).

Mito[Ca^{2+}] Increases in Young, Activated ISCs Promote H_2O_2 Generation Downstream of Electron Leak from ETC-CIII

Linked to their central role in energy metabolism, mitochondria are also an important site for ROS generation (Redza-Dutordoir and Averill-Bates, 2016; Schieber and Chandel, 2014; Yun and Finkel, 2014). Depending on their type, concentration, and spatial localization, ROS can promote mitohormesis and cell renewal (Yun and Finkel, 2014), act as signaling molecules (Schieber and Chandel, 2014), or cause oxidative damage and cell death (Redza-Dutordoir and Averill-Bates, 2016). ROS have emerged as conserved regulators of SC activity in flies, mice, and humans (Hochmuth et al., 2011; Paul et al., 2014; Tormos et al., 2011). However, the site and type of ROS generation, as well as how ROS signals influence ISC metabolism and activity, remains unclear.

One source for ROS is the mitochondrial ETC. In mammalian muscle tissue, Mito[Ca^{2+}] is posited to activate ETC CI/CIII, CIV, and CV (Glancy et al., 2013). The decrease in ATP/ADP ratios and increase in NADH/NAD+ ratios upon loss of Mito[Ca^{2+}] uptake are similar to the effect of ETC disruption (Figures S1A, S1B, S3E, and S3L), suggesting that Mito[Ca^{2+}] changes may influence ETC activity in young ISCs. To test this hypothesis, we asked whether Mito[Ca^{2+}] impacts ROS production from the ETC. We used variants of the genetically encoded ROS sensor RoGFP2 to identify hydrogen peroxide (H_2O_2) or glutathione redox potential (E_{GSH}) within the mitochondria of ISCs (Albrecht et al., 2011). Live imaging these sensors revealed that, consistent with previous reports using ROS-sensitive dyes (Hochmuth et al., 2011; Wang et al., 2014), young, quiescent ISCs possess low mitochondrial H_2O_2 (Mito[H_2O_2]) and E_{GSH} (Mito[E_{GSH}]), as respective MitoRoGFP2 recordings were only slightly lowered by treatment with the strong chemical reductant DTT (Figures S4A and S4B). However, following *Ecc15* challenge, Mito [H_2O_2] increased in young ISCs, rising during the peak of ISC activity (8 h and 16 h PI) and returning to baseline as ISCs returned to quiescence (24 h and 40 h PI; Figure 4A). Interestingly, Mito [E_{GSH}] was not elevated at 16 h post *Ecc15* infection (Figure S4C), highlighting that, consistent with other reports (Albrecht et al., 2011), H_2O_2 concentrations do not always correlate with the oxidation status of the glutathione system.

H_2O_2 can be generated as a consequence of electron leak from one of ten sites within the ETC (Brand, 2016; Brand et al., 2016; Orr et al., 2015; Quinlan et al., 2013). Of these, significant sites include the site IQ of CI and site IIIQo of CIII (Brand, 2016; Brand et al., 2016; Orr et al., 2015; Quinlan et al., 2013). Recently, compounds termed S1QELs and S3QELs were found to suppress electron leak from sites IQ and IIIQ, respectively, without impacting ETC flux (Brand et al., 2016; Orr et al., 2015). Feeding flies a prototypic member of each compound class, we observed that only S3QEL blocked increases in Mito[H_2O_2] following *Ecc15* infection (Figure 4B). S3QEL, but not S1QEL, also significantly reduced proliferation following infection, confirming that ROS are not merely by-products but instead support ISC activity, as predicted by previous studies (Hochmuth et al., 2011; Xu et al., 2017; Figure 4C). As expected, S3QEL feeding did not alter the NADH/NAD+ or ATP/ADP ratios of ISCs+EBs, which is consistent with the selective suppression of electron leakage without affecting ETC flux (Figures S4I and S4J). Together, these data suggest that in response to stress, electron leak from site IIIQ drives Mito[H_2O_2] generation and supports the activation of young ISCs.

Next, we asked whether increases in Mito[H_2O_2] require parallel increases in Mito[Ca^{2+}]. Using flies harboring ISC-specific MCU loss-of-function, we observed that following *Ecc15* infection, preventing Mito[Ca^{2+}] increases also suppressed Mito [H_2O_2] increases (Figures 4D and S4E). This relationship was not the case for other genetic conditions capable of inhibiting stress-induced proliferation (Figure S4D), which failed to block Mito[H_2O_2] increases (Figure 4D). They included knockdown of Stat (Buchon et al., 2009a, 2010; Jiang et al., 2009) or overexpression of dominant-negative Bsk (Bsk^{DN}) (Biteau et al., 2008; Biteau and Jasper, 2011; Tang et al., 2013). Mito[H_2O_2] increases are thus selectively dependent on Mito[Ca^{2+}] increases.

To ask whether Mito[Ca^{2+}] increases were also sufficient for Mito[H_2O_2] increases, we raised Mito[Ca^{2+}] by genetic or pharmacologic elevation of Cyto[Ca^{2+}] and probed changes in Mito [H_2O_2]. Interestingly, genetic conditions that elevated Mito [Ca^{2+}] (Figure 2E) also raised Mito[H_2O_2] (Figure 4E). Changes in Mito[H_2O_2] were driven by Mito[Ca^{2+}] rather than by Cyto [Ca^{2+}], as raising Cyto[Ca^{2+}] in the presence of MCU knockdown blocked increases in Mito[Ca^{2+}] (Figure 2E) and Mito[H_2O_2] (Figure 4F). Moreover, when MCU or hMCU overexpression accompanied increases in Cyto[Ca^{2+}], Mito[H_2O_2] rose to supraphysiologic levels. These included conditions whereby SERCA was pharmacologically inhibited by thapsigargin (Figure S4G) or when *Ecc15* infection drove ISC activation (Figures 4G, S4E, and S4F). In the presence of MCU overexpression, additional Mito[H_2O_2] still derived from site IIIQ, as S3QEL treatment restored Mito[H_2O_2] to those of unchallenged, control ISCs (Figure 4G and S4G). Of note, in the absence of perturbations elevating Cyto[Ca^{2+}], MCU or hMCU overexpression failed to cause an increase in Mito[H_2O_2] (Figure S4H). This finding suggested that both Cyto[Ca^{2+}] and MCU activity are limiting to elicit sufficient increases in Mito[Ca^{2+}] for the elevated production of Mito[H_2O_2]. Upon ISC activation, sustained increases in Cyto [Ca^{2+}] thus result in sustained elevation of Mito[Ca^{2+}], which in turn causes increased electron leak from ETC-CIII and downstream Mito[H_2O_2] production.

Mito[Ca^{2+}] Enhances ETC-CI Activity in Young ISCs

Rates of electron leak from CIII site Qo are strongly influenced by the activity of upstream ETC-CI and -CII. Because the loss of Mito [Ca^{2+}] uptake raises NADH/NAD+ ratios, suggesting a reduced capacity to oxidize NADH, we hypothesized that elevated Mito [Ca^{2+}] is required to stimulate optimal CI activity in young, activated ISCs. To test this hypothesis, we expressed Ndi1 in ISCs. Ndi1 is an alternative NADH dehydrogenase from yeast that, when ectopically expressed, can selectively rescue CI defects (Bahadorani et al., 2010; Bordt et al., 2017; Cho et al., 2012; Gaude et al., 2018; Sanz et al., 2010; Scialò et al., 2016). If elevated Mito[Ca^{2+}] is required for optimal CI activity, Ndi1 expression should rescue MCU loss-of-function phenotypes. Indeed, co-expression of Ndi1 completely restored ATP/ADP and NADH/NAD+ ratios (Figures 5A and 5B), as well as Mito [H_2O_2] in MCU^{DN}-expressing ISCs (Figure 5C). Ndi1 co-expression further fully rescued the proliferative defects caused by MCU^{DN} expression in young ISCs (Figure 5D). Of note, the individual expression of Ndi1 suppressed increases in Mito[H_2O_2] and concomitant ISC activity (Figures 5C and 5D). This finding is consistent with previous reports suggesting that in the absence of CI inhibition, lone expression of Ndi1 decreases ROS production (Bahadorani et al., 2010; Sanz et al., 2010). The rescue of MCU loss-of-function phenotypes was selective to Ndi1, as identical experiments performed using AOX (Fernandez-Ayala et al., 2009), an alternative oxidase capable of rescuing respiratory defects in CIII and CIV, failed to rescue ATP/ADP ratios, NADH/NAD+ ratios, Mito[H_2O_2], or proliferation (Figures S5A–S5D). Together, these data suggest a model whereby Mito[Ca^{2+}] activates CI during the activation of young ISCs (Figures 5E and 5F). This enhances NADH oxidation and ETC flux that in turn generates the ATP and ROS needed to sustain ISC proliferation.

Deficient Mito Ca^{2+} Uptake Contributes to a “Warburg-like” Metabolic Switch in Old ISCs

Our work so far identifies Mito[Ca^{2+}] increases as a link between signals that promote ISC activation by elevating Cyto[Ca^{2+}] and the metabolic adaption necessary to support ISC proliferation. This metabolic coupling by Mito[Ca^{2+}] appears defunct in old ISCs, which hence exhibit chronically low ATP/ADP ratios. An outstanding question, however, is how old ISCs can still support and maintain their chronic proliferative activity. In some cancer cell types, enhanced proliferative activity is supported by the Warburg effect, whereby even in the presence of oxygen (aerobic), glycolysis terminates at lactate dehydrogenase (Ldh) and mitochondria output is focused on the anabolic generation of lipids, amino acids, and nucleotides required for growth (DeBerardinis and Chandel, 2016; Vander Heiden and DeBerardinis, 2017). We hypothesized that such a metabolic switch might enable old ISCs to continue to proliferate, even when Mito [Ca^{2+}] is low and cannot promote ETC activity.

As a first step to investigate this hypothesis, we strove to compare the glycolytic and ETC activities of old and young ISCs.

Major sites of NADH oxidation include CI of the ETC and Ldh, which catalyzes the final step of aerobic glycolysis. To compare the relative activities of the ETC and aerobic glycolysis in young, quiescent and chronically active old ISCs, we aged flies using our 18°C model and live imaged the NADH/NAD+ ratios of progenitor cells following transient ETC or Ldh loss-of-function. Strikingly, disrupting ETC or Ldh activity yielded opposing phenotypes in old versus young progenitor cells: Levy RNAi or MCU^{DN} expression selectively raised the NADH/NAD+ ratios of young progenitor cells (Figures 6A and 6B), whereas Ldh RNAi selectively raised the NADH/NAD+ ratios of old progenitor cells (Figure 6A). Compared to young, quiescent ISCs, old chronically active ISCs may thus have switched their metabolism toward increased aerobic glycolysis.

To further test our hypothesis, we measured readouts for the ETC and glycolysis in young, quiescent; young, activated; and old chronically active ISCs. To readout glycolysis, we live imaged [lactate] in progenitor cells using Laconic, a recently developed fluorescence resonance energy transfer (FRET) sensor whose FRET signal decreases as [lactate] increases (Figure S6A; San Martín et al., 2013). To readout ETC activity, we examined mitochondrial membrane potential ($\Delta\Psi m$) by using the potentiometric dye tetramethylrhodamine ethyl ester (TMRE) (Rana et al., 2017). Supporting an age-dependent metabolic switch from the ETC to aerobic glycolysis, when compared to young, quiescent ISCs, [lactate] was higher in old chronically active ISCs, whereas $\Delta\Psi m$ modestly decreased (Figures 6E, 6F, and S6B). Increased [lactate] likely stemmed from an increased reliance on Ldh activity, as knockdown of Ldh significantly decreased [lactate] in old ISCs (Figure 6E). In contrast, when compared to young, quiescent ISCs; young, activated ISCs possessed higher [lactate] and $\Delta\Psi m$ (Figures 6C and 6D). This suggested that both aerobic glycolysis and ETC activation support the activation of young ISCs.

As a final readout, we monitored Mito[H_2O_2]. Consistent with age-dependent increases in ISC ROS levels reported by ourselves and others (Hochmuth et al., 2011; Hur et al., 2013; Iatsenko et al., 2018; Rera et al., 2011), Mito[H_2O_2] was slightly higher in old versus young ISCs (Figure S6C). However, unlike the large Mito[Ca^{2+}]-driven increases in Mito[H_2O_2] recorded during the activation of young ISCs (Figures 4 and S4), Mito[H_2O_2] in old ISCs correlated with low Mito [Ca^{2+}] (Figure 2I) and was insensitive to MCU loss-of-function (Figure S6C). Age-dependent increases in Mito[H_2O_2] and other ROS species may, therefore, derive from sources other than the ETC.

Together, our data suggest a model whereby young, quiescent ISCs possess low glycolytic and moderate ETC activities; young, activated ISCs possess high glycolytic and high ETC activities; whereas old chronically active ISCs possess high glycolytic and low ETC activities. Thus, while both active young and active old ISCs use aerobic glycolysis, older ISCs have undergone a larger Warburg-like metabolic switch to rely heavily on aerobic glycolysis in the absence of efficient ETC regulation by Mito[Ca^{2+}].

To further test this model, we reasoned that as much as ectopic Ndi1 expression rescued MCU loss-of-function phenotypes in young ISCs, expression of Ndi1 might rejuvenate the metabolism of old ISCs harboring low Mito[Ca^{2+}] and ETC-CI activity. We, therefore, aged flies using our 18C model and transiently expressed Ndi1 in old ISCs. Remarkably, Ndi1 expression restored the ATP/ADP ratios of old ISCs, suggesting a defect in ETC-CI activity in old ISCs (Figure 6G). Together, our data thus establish declining Mito[Ca^{2+}] uptake as a factor that contributes to an age-related Warburg-like switch in ISC metabolism.

Old ISCs Resemble ISCs Transformed by Oncogenes but Are Not Fully Metabolically Transformed

In some cancer cell types, the Warburg effect actively promotes cell proliferation (DeBerardinis and Chandel, 2016; Vander Heiden and DeBerardinis, 2017). We thus investigated whether such a Warburg-like metabolic switch contributes to the aberrant activity of old ISCs. Old ISCs lack efficient Mito[Ca^{2+}] uptake and possess low Mito[Ca^{2+}] and ATP/ADP ratios. Despite this, mitochondria Ca^{2+} uptake in old ISCs is not completely abolished, as MCU^{DN} expression further lowered the Mito[Ca^{2+}] and ATP/ADP ratios of old ISCs (Figures 2I and 7A). Surprisingly, knockdown of MCU or expression of MCU^{DN} enhanced the proliferative activity of old ISCs (Figures 7B and S7A). A Warburg-like switch in old ISCs may, therefore, contribute to aberrant proliferative activity, as enhancement of this switch by MCU loss-of-function accelerated ISC hyperplasia.

To explore the similarities between the metabolism of cancer cells and old ISCs directly, we examined the metabolism of ISCs transformed by transient expression of the oncogene Ras^{V12}. As an additional control, we also assessed ISCs expressing Hep, which, despite also driving chronic ISC activity, lacks the same oncogenic capacity as Ras^{V12} (Wang et al., 2013). Consistent with a dramatic shift to aerobic glycolysis upon oncogenic transformation, [lactate] was elevated in Ras^{V12}-expressing ISCs and increased to levels significantly higher than ISCs activated by *Ecc15* infection or Hep overexpression (Figure 7C). Higher [lactate] maybe a consequence of increased Ldh activity, as Ras^{V12} also increased the NADH/NAD+ ratios of ISCs+EBs (Figure S7B), which can activate Ldh (Hung et al., 2011). Moreover, as in old ISCs, Ras^{V12}-induced proliferation was also not supported by Mito [Ca^{2+}] (Figures 7D and S7C) and did not coincide with Mito [Ca^{2+}]-dependent increases in Mito[H_2O_2] (Figure S7D). This was contrasted by ISC activity induced by Hep overexpression or post *Ecc15* infection, of which each were strongly inhibited by MCU^{DN} expression (Figures 3C, 5D, 7D, and S5D). Oncogenic ISCs, however, appeared to have undergone a more comprehensive metabolic rewiring than old ISCs. Chronically active old ISCs and young, activated ISCs were energetically deficient, whereas Ras^{V12}-expressing ISCs harbored ATP/ADP ratios that were not significantly different from young, quiescent ISCs (Figure 7E) and were insensitive to MCU loss-of-function (Figure 7F).

Together, these data suggest that although both old ISCs and oncogenic ISCs have transitioned to rely heavily on aerobic glycolysis (Figure 7G), ISCs transformed by Ras^{V12} have undergone an additional metabolic rewiring step. This rewiring is characterized by exceptionally high [lactate] generation, high NADH/NAD+ ratios, low Mito[H_2O_2]

generation, the restoration of ATP/ADP ratios, and a total insensitivity to Mito[Ca^{2+}] uptake inhibition.

DISCUSSION

Our data identify an age-related metabolic reprogramming of ISCs that results in a metabolic profile that is reminiscent of transformed cells. In ISCs of young animals, we find that Mito [Ca^{2+}] serves as a critical coordinator of metabolic adaptation during transitions from quiescence to proliferation. This adaptation breaks down in old ISCs, which lack efficient Mito[Ca^{2+}] uptake and have undergone a Warburg-like metabolic switch that contributes to their deregulated proliferative activity. Our use of live-imaging approaches to investigate these metabolic transitions proved crucial to fully characterize ISC metabolism in their native context and to discover their metabolic reprogramming during aging. The fact that old ISCs resemble transformed cells metabolically is interesting, as it can be posited that such changes contribute to the age-related increase in cancer incidence in tissues like the gut.

Mito[Ca^{2+}] as a Central Coordinator of Metabolism in Young ISCs

Previous studies of *Drosophila* ISCs suggest important metabolic roles for aerobic glycolysis (Mattila et al., 2018; Schell et al., 2017), as well as lipolysis and fatty acid oxidation (Singh et al., 2016). Our work builds upon these genetic studies and by the extensive application of live imaging and metabolic reporters to outline a mechanism through which Mito[Ca^{2+}] coordinates metabolic adaptations during the activation of young ISCs.

We propose a model whereby the metabolic demands of young, quiescent ISCs are comparatively low and are supported by modest rates of glycolysis (Schell et al., 2017) and fatty acid oxidation (Singh et al., 2016). These pathways conclude in ATP generation by the ETC, the activity of which is fine-tuned by Mito[Ca^{2+}] increases that are accordingly brief and localized, as the MCU complex takes up Ca^{2+} from the cytosol into individual mitochondria. In support of this model, we find young, quiescent ISCs possess high ATP/ADP ratios, low [lactate], low [ROS], and modest $\Delta\Psi$m, as well as NADH/NAD+ ratios that are insensitive to *Ldh* knockdown, but are elevated by ETC or MCU loss-of-function.

The transient activation of young ISCs, however, is energetically demanding and correlates with sharp declines in ATP/ADP ratios. To support this demand, ISCs enhance energy generation through two mechanisms: lactate-generating aerobic glycolysis and increased ETC flux. The latter is coordinated by Mito[Ca^{2+}], which following ISC activation increases in tandem with Cyto[Ca^{2+}] (Deng et al., 2015; He et al., 2018; Xu et al., 2017) and enhances the activity of ETC-CI. This in turn increases rates of NADH oxidation to support metabolic demand and promotes electron leak from ETC-CIII to form Mito[H_2O_2]. Together, these coordinated metabolic adaptations ensure the restoration of ATP/ADP ratios as ISCs transition back to quiescence. Accordingly, loss of mitochondria Ca^{2+} uptake in young, activated ISCs results in the accumulation of NADH, a lack of Mito [H_2O_2] production, chronically low ATP/ADP ratios, and severely reduced proliferative activity. Additionally, consistent with a role for Mito[Ca^{2+}] in positively regulating ETC-CI activity, bypassing CI by expression of Ndi1 rescues phenotypes associated with MCU loss-of-function.

Our lineage-tracing experiments suggest a role for Mito [Ca^{2+}] in ISC to EC differentiation. Intriguingly, compared to ISCs, ECs possess a larger number of mitochondria with more matured cristae structures (Xu et al., 2018). ECs may thus rely upon high mitochondrial activity for their energetic needs, and the increased Mito[Ca^{2+}] and resulting ETC activity observed during the activation of young ISCs may function as a metabolic bridge between the comparatively low mitochondrial activity of quiescent ISCs and the higher mitochondrial activity of ECs.

Our data are consistent with a recent *Drosophila* study reporting that mitochondria from whole-fly preparations of MCU knockout animals possess lower ETC-CI-driven oxygen consumption (Tufi et al., 2019). How might Mito[Ca^{2+}] regulate CI activity? Ca^{2+} could allosterically regulate CI by binding to a matrix-exposed domain of 1 of the 40+ CI subunits. An intriguing candidate for direct regulation is the subunit NDUFAB1, which faces the matrix and carries a loosely conserved Ca^{2+}-binding EF-hand domain (Stroud et al., 2016; Triepels et al., 1999; Zhu et al., 2015). Alternatively, Ca^{2+} may indirectly regulate CI by a Ca^{2+}-sensitive regulatory protein, similar to the regulation of mammalian PDH by the Ca^{2+}-sensitive phosphatase PDP1 (Denton, 2009). Because CI is highly post-translationally modified (Carroll et al., 2005, 2013; Chen et al., 2004; Srinivas Bharath, 2017; Stram and Payne, 2016) and contains predicted Ca^{2+}/calmodulin-dependent protein kinase phosphorylation sites (Gowthami et al., 2019), it will be interesting to identify modifications that are regulated by Ca^{2+}.

An outstanding question from our work is what fuels the ETC during periods of high energetic demand? Mitochondrial pyruvate oxidation may not be a significant source. Unlike disruptions in MCU or ETC activity, knockdown of MPC1 or PDH-1a fails to impact the cytosolic ATP/ADP or NADH/NAD+ ratios of young, quiescent or active ISCs. Moreover, disruptions in mitochondrial pyruvate oxidation are reported to enhance, rather than suppress, ISC proliferation (Mattila et al., 2018; Schell et al., 2017). The ETC may thus be fueled by other pathways, including fatty acid oxidation (Singh et al., 2016) or by NADH generated during glycolysis, which can enter the mitochondria by the malate:aspartate shuttle (Davila et al., 2018).

Warburg-like Reprogramming of SCs in Aging and Cancer

Data from both model organisms and human patients implicate Warburg-like metabolic switches in aging and cancer. Our work ties these metabolic changes to age-related declines in SC function. Aging is the most potent risk factor in cancer development, with greater than 60% of human cancers occurring in patients over 65 (Frank, 2007). In recent years, increasing evidence supports the so-called “geroncogenesis” hypothesis of cancer development, whereby metabolic changes precede and contribute to oncogenic transformations and tumorigenesis (Wu et al., 2014). Intriguingly, we find the Warburg-like shifts of old ISCs actively enhance ISC hyperplasia and are reminiscent of oncogenic ISCs (Figure 7). Given the surprising level of genetic instability present in aging ISCs (Siudeja et al., 2015), it will be interesting to investigate whether our observed Mito[Ca^{2+}]-driven metabolic changes in aging ISCs precede or accompany the accumulation of somatic mutations.

A broader unresolved question stemming from our work concerns why old ISCs lack efficient Mito[Ca^{2+}] uptake. One possibility is that old ISCs, which possess chronically high Cyto[Ca^{2+}], downregulate MCU activity to avoid Mito[Ca^{2+}] overload and cell death (Choi et al., 2017; von Stockum et al., 2015). In independent RNA sequencing (RNA-seq) studies, however, we have not observed age-related downregulation of transcripts for any of the major players in Mito[Ca^{2+}] homeostasis (dMCU, dMICU1, dMICU3, dEMRE, and dNCLX). It will, therefore, be interesting in future work to dissect the post-translational regulation of the MCU complex in aging ISCs.

It is striking that age-dependent metabolic changes may be reversible. The fact that expression of Ndi1 can rejuvenate the energy status of old ISCs possessing low Mito[Ca^{2+}] provides a possible mechanism for the previously observed lifespan extension in flies expressing Ndi1 in intestinal progenitor cells (Hur et al., 2013). More broadly, restoring ETC activity has beneficial effects in aging and cancer. Successful aging interventions, such as calorie restriction and exercise, improve ETC function (Choi et al., 2011; Guarente, 2008; Joseph et al., 2016), whereas both transgenic and pharmacological manipulations, including Ndi 1 expression (Santidrian et al., 2013), have been found to decrease cancer growth, both *in vitro* and *in vivo* (Urra et al., 2017). Thus, it will be interesting to examine interactions between Mito[Ca^{2+}] and ETC function during these interventions, particularly because alterations in MCU expression are associated with age-related diseases, such as pulmonary arterial hypertension (Hong et al., 2017) and breast and liver cancers (Hall et al., 2014; Ren et al., 2017; Tosatto et al., 2016).

STAR★METHODS

RESOURCE AVAILABILITY

Lead contact—Further information and requests for resources and reagents should be directed to and will be fulfilled by the Lead Contact, Heinrich Jasper (jasperh@gene.com).

Materials availability—Publicly available fly lines (VDRC, BDSC) should be requested directly to the corresponding repositories: https://stockcenter.vdrc.at/control/main, https://bdsc.indiana.edu, https://kyotofly.kit.jp. Fly lines and plasmid constructs generated in this study can be requested without restriction upon an agreement with a material transfer agreement (MTA).

Data and code availability—Image analysis functions and scripts written in Python and imagej macro programming languages can be found at https://github.com/morriso1. No datasets were generated in this study.

EXPERIMENTAL MODEL AND SUBJECT DETAILS

***Drosophila* stocks—**The following fly lines were obtained from Bloomington *Drosophila* Stock Center: UAS::MitoRoGFP2_Orp1 (BL67667), UAS::MitoRoGFP2_Grx1 (BL67664), UAS::SERCA^{RNAi} (BL44581), UAS::Stim^{RNAi} (BL27263), UAS::TrpA1^{RNAi} (BL31504), UAS::Ras^{V12} (BL64196), esg::G4, Tub::G80ts (BL7017, BL7108), UAS::MitoGFP (BL84977) The following fly lines were obtained from VDRC stock center:

UAS::MCU^{RNAi} (v110781), UAS::Stat^{RNAi} (v106980), UAS::levy^{RNAi} (v101523), UAS::PDH-E1a^{RNAi} (v107209), UAS::MPC1^{RNAi} (v15858), UAS::Ldh^{RNAi} (v31192), UAS:Mdh1^{RNAi} (v110604). The UAS::MitoTdTomato fly line was obtained from Kyoto stock center (DGRC #117016). The following fly lines were kind gifts: UAS::LacZ^{RNAi} from Masayuki Miura (University of Tokyo), UAS::MCU^{DN} from Ronald Davies (The Scripts Institute Florida, USA); UAS::MCU, UAS::hMCU and MCU^{52} from Jongkyeong Chung (Seoul National University, Korea); UAS::MitoGCaMP3 from Fumiko Kawasaki (Pennsylvania State University, USA); UAS::Stim and UAS::Orai from G. Hasan (Tata Institute of Fundamental Research, India); UAS::Bsk^{DN}, UAS::Hepfrom Marek Mlodzik (Icahn School of Medicine, USA); Su(H)GBE::G80 from Steven Hou (National Cancer Institute, USA); UAS::Ndi1 and UAS::AOX from Howard T. Jacobs (University of Tampere, Finland). A full list of fly genotypes used in each figure panel is available in Table S1.

Fly husbandry—Flies were raised on standard yeast/molasses food containing 13.8 g agar, 22 g molasses, 75 g malt extract, 18 g dry inactivated yeast, 80 g corn flour, 10 g soy flour, 6.25 ml, propionic acid, 2 g methyl 4-hydroxybenzoate, 7.2 mL ethanol (200 proof) and water up to 1 L. Unless otherwise noted, flies were maintained at 25°C and 65% humidity on a 12 h light/dark cycle.

METHOD DETAILS

Cloning and transgenic fly generation—CEPIA3mt cDNA was cloned into pUAST vector via standard restriction cloning and injected in w1118 embryos via standard procedures (Rainbow Transgenics). SoNaR was amplified from pCDNA3.1-SoNaR using primers Fw: GGTACCatgaaccggaagtggggcc and Rev: cgggaggagatgatgggctagGAATTC. cpYFP was amplified from pCDNA3.1-cpYFP using primers Fw: GGTACCatgtacaacagcgacaacgtct and Rev: gggcacaagctggagtacaactagGAATTC. Amplified fragments were then cloned into a modified pUAST_AttB vector using EcoR1 and Kpn1 restriction enzyme sites and injected into flies harboring the Attp2 landing site via standard procedures (BestGene). PercevalHR, Laconic and Mito-R-GECO1 were synthesized and cloned into pUAST_AttB vector by Genentech BioMedical Resources Department and injected into flies harboring the Attp2 (PercevalHR and Laconic) or VK00037 landing sites via standard procedures (WellGenetics). The miRNA targeting MCU was designed as in Chen et al. (2007). To construct the UAS::MCU^{miRNA} line, the following sequence targeting MCU exon FBgn0042185_FBgn0042185:5 was synthesized, cloned in pUAST and injected in w1118 embryos via standard procedures (Rainbow Transgenic):

GGCCGAATTCATGTTTAAAGTCCACAACTCATCAAGGAAAATGAAAGTCAAAGTT
GGCAGCTTACTTAAACTTAATCACAGCCTTTAATGTCGACCACCACCACCCATAGC
AGTAAGTTAATATACCATATCTACTTCTATGGGTGGTGGTGGTCGGTACCTAAAGTG
CCTAACATCATTATTTAATTTTTTTTTTTTTTGGCACACGAATAACCATGCCGTTTTG
CGGCCGCGGCC

***Drosophila* TARGET system, aging and MARCM induction—**We used the TARGET system for conditional expression of UAS-linked transgenes (Brand and Perrimon, 1993; McGuire et al., 2004). Conditional expression in ISCs + EBs was achieved by combining ISC + EB driver esg::Gal4 (esg::G4) with Gal80ts (G80ts), a temperature-sensitive Gal4 inhibitor driven by a tubulin promoter (Tub::G80ts). For conditional expression in only ISCs, esg::Gal4 and Tub::Gal80ts were additionally combined with Su(H)GBE-G80, which drives the expression of a temperature-insensitive version of Gal80 in EBs (Wang et al., 2014). When using the TARGET system, flies were initially cultured at 18°C to avoid transgene expression. Progeny from these crosses were collected and allowed to mate at 18°C for two days. Mated female progeny were kept at 18°C for at least one further day before being shifted to the restrictive temperature of 29°C for the indicated time to induce transgene expression.

For experiments using our 18°C aging model, flies were kept at 18°C for at least 60 days before shifting to 29°C to induce transgene expression. Food was changed once a week. For experiments using our 29°C aging model, flies were kept at 29°C for at least 30 days. Food was changed every 2-3 days.

For activation of MARCM clones, flies were heat-shocked at 37°C for 45 min. Following heat-shock, flies were kept at 25°C and dissected after 10 days.

Ecc15 infection experiments and S1QEL/S3QEL/Thapsigargin/Rotenone/Oligomycin treatments—_Ecc15_ cultures in Luria Broth (LB) were initiated from single colonies grown on rifampicin plates. Following 16 – 20 h at 29C with agitation, cultures were centrifuged and a concentrated bacterial pellet (OD of ≈200) was resuspended 1:1 with 5% sucrose to yield an _Ecc15_ infection solution. Flies were starved for 2 h at 29°C and then transferred to fresh vials covered with a filter paper (WhatmanTM) and either 150 µL of _Ecc15_ infection solution or 2.5% sucrose (mock) solution. For time-course experiments, flies were left on _Ecc15_ saturated filter paper for 2 h before being transferred onto fresh food. For all other infection experiments, flies remained on _Ecc15_ saturated filter paper until dissection at a 16 h time point.

As previously (Brand et al., 2016), for S1QEL/S3QEL treatments, flies were starved for 4 h at 29°C to synchronize feeding and transferred to 5% sucrose containing 0.8% DMSO, 0.8 µM S1QEL1.1 or S3QEL2. After 24 h, flies were starved for 2 h at 29°C in vials containing 0.8% DMSO, 0.8 µM S1QEL1.1 or S3QEL2 but without sucrose. For _Ecc15_ experiments, flies were then fed 2.5% sucrose solutions supplemented with: 0.8% DMSO, 0.8% DMSO + _Ecc15_, 0.8 µM S1QEL1.1 + _Ecc15_, 0.8 µM S3QEL2 or 0.8 µM S3QEL2 + _Ecc15_. For thapsigargin (TG) experiments, flies were instead fed 2.5% sucrose solutions supplemented with: 0.8% DMSO, 0.8% DMSO + 0.5 µM TG, 0.8 µM S3QEL2 + 0.5 TG µM. For experiments using respiratory poisons, flies were starved for 4 h at 29°C to synchronize feeding and transferred to 5% sucrose containing 2% ethanol, 50 µM rotenone or 30 µM Oligomycin.

Immunohistochemistry and antibodies—Female fly midguts were dissected in PBS and fixed for 1 h at room temperature in a solution containing: 4% formaldehyde in a pH 7.5 solution containing 100 mM glutamic acid, 25 mM KCl, 20 mM $MgSO_4$, 4 mM sodium phosphate dibasic, 1 mM $MgCl_2$. Guts were then washed briefly in PBS and blocked on a shaker with wash buffer (1 × PBS, 0.5% bovine serum albumin and 0.1% Triton X-100), first for 30 min at room temperature, followed by 1 h at 4°C. Rabbit anti-phospho-Histone H3 (EMD Millipore – 1:5000), mouse anti-Prospero (DSHB MR1A – 1:200), rabbit anti-PDM1 (gift from Xiaohang Yang at Zhejiang University – 1:300), or mouse anti-Delta (DSHB C594.9B – 1:100 dilution) primary antibodies were incubated overnight at 4C (1:5000,1:100 dilutions respectively). Fluorescent secondary antibodies from Jackson Immunoresearch were incubated for 4 h at room temperature (1:500 dilution). Antibodies were diluted in wash buffer. Hoechst was used to stain DNA. Fixed samples were imaged using a 3i W Spinning Disc Confocal.

***Ex vivo* Drosophila intestine imaging setup—**Flies were dissected in Adult Hemolymph-like Saline (AHLS) culture media containing 2mM $CaCl_2$, 5mM KCl, 5mM HEPES, 8.2mM MgCl2, 108mM NaCl, 4mM $NaHCO_3$, 1mM NaH_2PO_4, 5mM Trehalose and 10 mM Sucrose. Guts were rapidly transferred to 35 mm glass bottom dishes (MatTek, P35G-1.5-14-C), embedded in 3% low melting agarose (in AHLS) and submerged in AHLS. For all experiments except Figure S6A, guts were fully embedded. In Figure S6A, guts were embedded only at their very anterior and posterior regions. This ‘exposed’ setup enabled the temporal addition of [Lactate] during live-imaging.

Image acquisition—For all experiments except Laconic FRET imaging, identical sized z stacks covering a single layer of the *Drosophila* epithelium were imaged using either a 40X PlanFluor oil NA 1.3 or 63X PlanAPO Oil NA 1.4 objective attached to a 3i W Spinning Disc Confocal possessing a Zeiss AxioObserver M1 inverted microscope, Yokogawa W1 spinning disc unit and Photometrics Evolve EMCCD and Hamamatsu FLASH 4.0 sCMOS cameras. In Figures 2D and 2I, an additional 2X magnification changer was applied. For Mito [Ca^{2+}] movies, z stacks were recorded every 6 s for 12 mins. For ratiometric PercevalHR, SoNaR, cpYFP, MitoRoGFP2_Orp1 and MitoRoGFP2_Grx1 biosensors, probe fluorescence was excited sequentially using the 405 nm and 488 nm laser lines and emission was detected at 500-550 nm. Imaging settings were carefully optimized prior to each experiment to ensure optimal dynamic range without saturating cameras.

Test experiments with the MitoRoGFP2_Orp1 and MitoRoGFP2_Grx1 biosensors were performed after incubating dissected midgut tissue with 10mM DTT or 1 mM Diamide (in AHLS) for 10 mins (Albrecht et al., 2011). Note, the imaging setting for these test experiments were not identical to those used in other experiments and thus possess comparatively lower 405/488 nm ratios.

For experiments measuring $\Delta\Psi m$, dissected guts were incubated for 15 min in AHLS containing 75 nM TMRE and rinsed briefly in AHLS containing 20 nM TMRE. Guts were then mounted similarly to all other live-imaging experiments, but an additional 20 nM TMRE was added into the agarose and submerging AHLS. MitoGFP and TMRE were sequentially excited at 488 nm and 561 nm, respectively.

For Laconic imaging experiments, identical sized z stacks covering a single layer of the *Drosophila* epithelium were imaged using a 40X PlanFluor oil NA 1.3 objective attached to Nikon Ti-E Spinning Disc Confocal possessing a Photometrics Prime95B camera. Following excitation using the 440 nm laser line, emission was sequentially detected at 460-500 nm and 530-570 nm.

For Cyto[Ca^{2+}] imaging experiments, identical sized z stacks covering a single layer of the *Drosophila* epithelium were imaged using a Zeiss LSM 7MP two-photon microscope equipped with a Chameleon XR laser (Coherent, Santa Clara, CA) running at 950nm and using a W Plan-Apochromat 20 × 1.0NA lens. GCaMP3 emission was captured at 500–550 nm and mCherry emission at 575–610 nm. For Cyto[Ca^{2+}] movies, z stacks were recorded every 8 s for 13.3 mins.

QUANTIFICATION AND STATISTICAL ANALYSIS

Image pre-processing—Live-imaging recordings of MitoGCaMP3, CEPIA3mt, MitoTdTomato, Mito-R-GECO1, PercevalHR, SoNaR, cpYFP, MitoRoGFP2_Orp1, MitoRoGFP2_Grx1 or TMRE were analyzed using custom Python or ImageJ macro scripts. For all experiments except those measuring ΔΨm, z stack images were converted to mean intensity projections and where required, background was subtracted using a rolling ball algorithm. In experiments measuring ΔΨm, to avoid detecting overlapping TMRE signal from basal visceral muscle cells or apical ECs, single z-slice images intersecting the center of MitoGFP labeled ISCs were analyzed.

Image segmentation and intensity quantifications—Automated segmentation was performed using classical algorithms (e.g., Li, Otsu etc.), machine-learning based segmentation tools such as Ilastik or trainable WEKA (Arganda-Carreras et al., 2017; Berg et al., 2019), or deep-learning based segmentation tools such Stardist and Cellpose (Schmidt et al., 2018, MICCAI, conference; Stringer et al., 2020; Weigert et al., 2020, WACV, conference). Automated segmentation and ROI detection were carefully optimized so that each ROI approximately represents a single cell. When sensors were expressed using esg::G4 in the absence of Su(H)GBE::G80ts, thresholding was optimized so as to only segment smaller cells that likely represent ISCs and early-stage EBs. Larger esg::G4 positive cells, which are probably late-stage EBs that are soon approaching differentiation into ECs, were excluded from analysis. Mean intensity measurements within ROIs were compiled and analyzed using custom Python scripts (https://github.com/morriso1).

For Mito[Ca^{2+}] measurements in Figures S2A and S2B, images were automatically segmented using the MitoGCaMP3 channel and mean intensity measurements were made within automatically drawn regions of interest (ROIs). For other Mito[Ca^{2+}] measurements, MitoTdTomato or MitoGFP was used to normalize for reporter expression and mitochondrial morphology. Accordingly, the MitoTdTomato or MitoGFP channel was used for automated image segmentation and ROIs detection. Mean intensity measurements were then made in the ROIs of MitoGCaMP3/MitoTdTomato, CEPIA3mt/MitoTdTomato or Mito-R-GECO1/MitoGFP channels.

For ratiometric measurements of PercevalHR, SoNaR, cpYFP, MitoRoGFP2_Orp1 and MitoRoGFP2_Grx1, the 488 nm excitation channel was used for automated image segmentation and ROIs detection. Mean intensity measurements were then made in the ROIs of both 405 nm and 488 nm excitation channels. For experiments measuring ΔΨm, MitoGFP was used for automated image segmentation and ROIs detection. Mean intensity measurements of all detected ROIs were then made in the TMRE channel. For ratiometric FRET measurements of Laconic, the 530-570 nm emission channel was used for automated image segmentation and ROIs detection. Mean intensity measurements were then made in the ROIs of both the 460-500 nm and 530-570 nm emission channels.

To create false color ratio images, mean intensity projections were first converted from 16 to 32-bit format. Following automated image segmentation, background pixels were assigned to Not a Number (NaN) and a ratio image was generated via pixel by pixel division of numerator and denominator images. Ratio images were displayed in false color using the ImageJ “fire” LookUp Table (LUT) or matplotlib “magma” LUT.

For Cyto[Ca^{2+}] imaging, z stack images were converted to mean intensity projections, and automatic image stabilization, background subtraction, image segmentation and ROI detection was performed using Image Analyst MKII (Image Analyst Software, Novato, CA). Mean intensity traces were then measured over time in each ROI. Oscillation patterns were calculated in an unsupervised, automated manner using MATLAB. Mean intensity traces were smoothed using a Savitzky-Golay filter and peaks were identified using the “findpeaks” algorithm from the MATLAB Signal Processing Toolbox.

MARCM cell lineage analysis—For MARCM clone analysis, individual channels of multi-channel images were automatically segmented using machine-learning based segmentation tools such as Ilastik or trainable WEKA (Arganda-Carreras et al., 2017; Berg et al., 2019), or deep-learning based segmentation tools such as Stardist and Cellpose (Schmidt et al., 2018, MICCAI, conference; Stringer et al., 2020; Weigert et al., 2020, WACV, conference). A custom Python library (https://github.com/morriso1/cell_counting_analysis) was then used to measure the colocalization of each segmented DAPI+ nuclei to other segmented channel markers. Colocalization between segmented DAPI + nuclei and segmented GFP+ clones determined whether a cell was inside or outside of a clone.

Analysis of Laconic time-lapse imaging—Movies were registered using the ‘rigid body’ transformation option from Python’s pyStackReg package. Laconic’s 530-570 nm emission channel was used for image segmentation. Movie frames were individually segmented using Python’s Scikit-image module and individual ROIs were tracked using Python’s TrackPy. Mean intensity measurements were then made in each frame in the ROIs of both channels using Python’s Scikit-image package.

Statistical Methods—Statistical analysis was performed using Python scipy and scikit-posthoc packages. Statistical methods used and sample sizes are listed in Figure Legends and Table S1. For PH3 and MARCM count data, data passed D’Agostino & Pearson normality test ($p < 0.05$) and statistical significance was calculated via parametric tests. For all other experiments, data did not pass D’Agostino & Pearson normality test ($p > 0.05$) and statistical significance was calculated via non-parametric tests. Graphs were generated using Python matplotlib and seaborn packages. All figure panels are representative of at least two independent experiments performed on different days.

Supplementary Material

Refer to Web version on PubMed Central for supplementary material.

ACKNOWLEDGMENTS

We thank Masayuki Miura, Ronald Davies, Jongkyeong Chung, Fumiko Kawasaki, Gaiti Hasan, Marek Mlodzik, Steven Hou, Howard T. Jacobs, the Vienna Drosophila RNAi Center, the Kyoto Stock Center, and the Bloomington Stock Center for flies. We thank Akos Gerencser (Buck Institute for Research on Aging) and Meredith Sagolla (Genentech Center for Advanced Light Microscopy) for microscopy assistance and advice. O.M. was supported by an EMBO Long-Term Postdoctoral Research Fellowship (ALTF 998-2016). Work in the H.J. lab at the Buck Institute for Research on Aging was supported by NIH RO1 GM117412. We thank past and present Jasper Lab members for invaluable discussion and critique.

REFERENCES

Albrecht SC, Barata AG, Grosshans J, Teleman AA, and Dick TP (2011). In vivo mapping of hydrogen peroxide and oxidized glutathione reveals chemical and regional specificity of redox homeostasis. Cell Metab. 14, 819–829. [PubMed: 22100409]

Arganda-Carreras I, Kaynig V, Rueden C, Eliceiri KW, Schindelin J, Cardona A, and Sebastian Seung H (2017). Trainable Weka Segmentation: a machine learning tool for microscopy pixel classification. Bioinformatics 33, 2424–2426. [PubMed: 28369169]

Bahadorani S, Cho J, Lo T, Contreras H, Lawal HO, Krantz DE, Bradley TJ, and Walker DW (2010). Neuronal expression of a single-subunit yeast NADH-ubiquinone oxidoreductase (Ndi1) extends Drosophila lifespan. Aging Cell 9, 191–202. [PubMed: 20089120]

Baughman JM, Perocchi F, Girgis HS, Plovanich M, Belcher-Timme CA, Sancak Y, Bao XR, Strittmatter L, Goldberger O, Bogorad RL, et al. (2011). Integrative genomics identifies MCU as an essential component of the mitochondrial calcium uniporter. Nature 476, 341–345. [PubMed: 21685886]

Bensard CL, Wisidigama DR, Olson KA, Berg JA, Krah NM, Schell JC, Nowinski SM, Fogarty S, Bott AJ, Wei P, et al. (2019). Regulation of Tumor Initiation by the Mitochondrial Pyruvate Carrier. Cell Metab. 31, 284–300.e7. [PubMed: 31813825]

Berg S, Kutra D, Kroeger T, Straehle CN, Kausler BX, Haubold C, Schiegg M, Ales J, Beier T, Rudy M, et al. (2019). ilastik: interactive machine learning for (bio)image analysis. Nat. Methods 16, 1226–1232. [PubMed: 31570887]

Biteau B, and Jasper H (2011). EGF signaling regulates the proliferation of intestinal stem cells in Drosophila. Development 138, 1045–1055. [PubMed: 21307097]

Biteau B, Hochmuth CE, and Jasper H (2008). JNK activity in somatic stem cells causes loss of tissue homeostasis in the aging Drosophila gut. Cell Stem Cell 3, 442–455. [PubMed: 18940735]

Bordt EA, Clerc P, Roelofs BA, Saladino AJ, Tretter L, Adam-Vizi V, Cherok E, Khalil A, Yadava N, Ge SX, et al. (2017). The Putative Drp1 Inhibitor mdivi-1 Is a Reversible Mitochondrial Complex I Inhibitor that Modulates Reactive Oxygen Species. Dev. Cell 40, 583–594.e6. [PubMed: 28350990]

Brand MD (2016). Mitochondrial generation of superoxide and hydrogen peroxide as the source of mitochondrial redox signaling. Free Radic. Biol. Med 100, 14–31. [PubMed: 27085844]

Brand AH, and Perrimon N (1993). Targeted gene expression as a means of altering cell fates and generating dominant phenotypes. Development 118, 401–415. [PubMed: 8223268]

Brand MD, Goncalves RL, Orr AL, Vargas L, Gerencser AA, Borch Jensen M, Wang YT, Melov S, Turk CN, Matzen JT, et al. (2016). Suppressors of Superoxide-H_2O_2 Production at Site I_Q of Mitochondrial Complex I Protect against Stem Cell Hyperplasia and Ischemia-Reperfusion Injury. Cell Metab. 24, 582–592. [PubMed: 27667666]

Bricker DK,Taylor EB, Schell JC, Orsak T, Boutron A, Chen YC, Cox JE, Cardon CM, Van Vranken JG, Dephoure N, et al. (2012). A mitochondrial pyruvate carrier required for pyruvate uptake in yeast, Drosophila, and humans. Science 337, 96–100. [PubMed: 22628558]

Buchon N, Broderick NA, Chakrabarti S, and Lemaitre B (2009a). Invasive and indigenous microbiota impact intestinal stem cell activity through multiple pathways in Drosophila. Genes Dev. 23, 2333–2344. [PubMed: 19797770]

Buchon N, Broderick NA, Poidevin M, Pradervand S, and Lemaitre B (2009b). Drosophila intestinal response to bacterial infection: activation of host defense and stem cell proliferation. Cell Host Microbe 5, 200–211. [PubMed: 19218090]

Buchon N, Broderick NA, Kuraishi T, and Lemaitre B (2010). Drosophila EGFR pathway coordinates stem cell proliferation and gut remodeling following infection. BMC Biol. 8, 152. [PubMed: 21176204]

Cao C, Wang S, Cui T, Su XC, and Chou JJ (2017). Ion and inhibitor binding of the double-ring ion selectivity filter of the mitochondrial calcium uniporter. Proc. Natl. Acad. Sci. USA 114, E2846–E2851. [PubMed: 28325874]

Carroll J, Fearnley IM, Skehel JM, Runswick MJ, Shannon RJ, Hirst J, and Walker JE (2005). The post-translational modifications of the nuclear encoded subunits of complex I from bovine heart mitochondria. Mol. Cell. Proteomics 4, 693–699. [PubMed: 15728260]

Carroll J, Ding S, Fearnley IM, and Walker JE (2013). Post-translational modifications near the quinone binding site of mammalian complex I. J. Biol. Chem 288, 24799–24808. [PubMed: 23836892]

Chandel NS, Jasper H, Ho TT, and Passegué E (2016). Metabolic regulation of stem cell function in tissue homeostasis and organismal ageing. Nat. Cell Biol 18, 823–832. [PubMed: 27428307]

Chen R, Fearnley IM, Peak-Chew SY, and Walker JE (2004). The phosphorylation of subunits of complex I from bovine heart mitochondria. J. Biol. Chem 279, 26036–26045. [PubMed: 15056672]

Chen CH, Huang H, Ward CM, Su JT, Schaeffer LV, Guo M, and Hay BA (2007). A synthetic maternal-effect selfish genetic element drives population replacement in Drosophila. Science 316, 597–600. [PubMed: 17395794]

Cho J, Hur JH, Graniel J, Benzer S, and Walker DW (2012). Expression of yeast NDI1 rescues a Drosophila complex I assembly defect. PLoS One 7, e50644. [PubMed: 23226344]

Choi JS, Choi KM, and Lee CK (2011). Caloric restriction improves efficiency and capacity of the mitochondrial electron transport chain in Saccharomyces cerevisiae. Biochem. Biophys. Res. Commun 409, 308–314. [PubMed: 21575595]

Choi S, Quan X, Bang S, Yoo H, Kim J, Park J, Park KS, and Chung J (2017). Mitochondrial calcium uniporter in *Drosophila* transfers calcium between the endoplasmic reticulum and mitochondria in oxidative stress-induced cell death. J. Biol. Chem 292, 14473–14485. [PubMed: 28726639]

Colca JR, McDonald WG, Cavey GS, Cole SL, Holewa DD, Brightwell-Conrad AS, Wolfe CL, Wheeler JS, Coulter KR, Kilkuskie PM, et al. (2013). Identification of a mitochondrial target of thiazolidinedione insulin sensitizers (mTOT)–relationship to newly identified mitochondrial pyruvate carrier proteins. PLoS One 8, e61551. [PubMed: 23690925]

Davila A, Liu L, Chellappa K, Redpath P, Nakamaru-Ogiso E, Paolella LM, Zhang Z, Migaud ME, Rabinowitz JD, and Baur JA (2018). Nicotinamide adenine dinucleotide is transported into mammalian mitochondria. eLife 7, e33246. [PubMed: 29893687]

De Stefani D, Raffaello A, Teardo E, Szabò I, and Rizzuto R (2011). A forty-kilodalton protein of the inner membrane is the mitochondrial calcium uniporter. Nature 476, 336–340. [PubMed: 21685888]

DeBerardinis RJ, and Chandel NS (2016). Fundamentals of cancer metabolism. Sci. Adv 2, e1600200. [PubMed: 27386546]

Deng H, Gerencser AA, and Jasper H (2015). Signal integration by Ca(2+) regulates intestinal stem-cell activity. Nature 528, 212–217. [PubMed: 26633624]

Denton RM (2009). Regulation of mitochondrial dehydrogenases by calcium ions. Biochim. Biophys. Acta 1787, 1309–1316. [PubMed: 19413950]

Drago I, and Davis RL (2016). Inhibiting the Mitochondrial Calcium Uniporter during Development Impairs Memory in Adult Drosophila. Cell Rep 16, 2763–2776. [PubMed: 27568554]

Fernandez-Ayala DJ, Sanz A, Vartiainen S, Kemppainen KK, Babusiak M, Mustalahti E, Costa R, Tuomela T, Zeviani M, Chung J, et al. (2009). Expression of the Ciona intestinalis alternative oxidase (AOX) in Drosophila complements defects in mitochondrial oxidative phosphorylation. Cell Metab. 9, 449–460. [PubMed: 19416715]

Frank SA (2007). Dynamics of Cancer: Incidence, Inheritance, and Evolution (Princeton University Press).

Gaude E, Schmidt C, Gammage PA, Dugourd A, Blacker T, Chew SP, Saez-Rodriguez J, O'Neill JS, Szabadkai G, Minczuk M, et al. (2018). NADH Shuttling Couples Cytosolic Reductive Carboxylation of Glutamine with Glycolysis in Cells with Mitochondrial Dysfunction. Mol. Cell 69, 581–593.e587. [PubMed: 29452638]

Giorgi C, Marchi S, and Pinton P (2018). The machineries, regulation and cellular functions of mitochondrial calcium. Nat. Rev. Mol. Cell Biol 19, 713–730. [PubMed: 30143745]

Glancy B, and Balaban RS (2012). Role of mitochondrial Ca2+ in the regulation of cellular energetics. Biochemistry 51, 2959–2973. [PubMed: 22443365]

Glancy B, Willis WT, Chess DJ, and Balaban RS (2013). Effect of calcium on the oxidative phosphorylation cascade in skeletal muscle mitochondria. Biochemistry 52, 2793–2809. [PubMed: 23547908]

Gowthami N, Sunitha B, Kumar M, Keshava Prasad TS, Gayathri N, Padmanabhan B, and Srinivas Bharath MM (2019). Mapping the protein phosphorylation sites in human mitochondrial complex I (NADH: Ubiquinone oxidoreductase): A bioinformatics study with implications for brain aging and neurodegeneration. J. Chem. Neuroanat 95, 13–28. [PubMed: 29499254]

Gu H, Chen C, Hao X, Su N, Huang D, Zou Y, Lin SH, Chen X, Zheng D, Liu L, et al. (2020). MDH1-mediated malate-aspartate NADH shuttle maintains the activity levels of fetal liver hematopoietic stem cells. Blood 136, 553–571. [PubMed: 32396938]

Guarente L (2008). Mitochondria–a nexus for aging, calorie restriction, and sirtuins? Cell 132, 171–176. [PubMed: 18243090]

Guo L, Karpac J,Tran SL, and Jasper H (2014). PGRP-SC2 promotes gut immune homeostasis to limit commensal dysbiosis and extend lifespan. Cell 156, 109–122. [PubMed: 24439372]

Hall DD, Wu Y, Domann FE, Spitz DR, and Anderson ME (2014). Mitochondrial calcium uniporter activity is dispensable for MDA-MB-231 breast carcinoma cell survival. PLoS One 9, e96866. [PubMed: 24802861]

He L, Si G, Huang J, Samuel ADT, and Perrimon N (2018). Mechanical regulation of stem-cell differentiation by the stretch-activated Piezo channel. Nature 555, 103–106. [PubMed: 29414942]

Herbener GH (1976). A morphometric study of age-dependent changes in mitochondrial population of mouse liver and heart. J. Gerontol 31, 8–12. [PubMed: 1244408]

Herzig S, Raemy E, Montessuit S, Veuthey JL, Zamboni N, Westermann B, Kunji ER, and Martinou JC (2012). Identification and functional expression of the mitochondrial pyruvate carrier. Science 337, 93–96. [PubMed: 22628554]

Hochmuth CE, Biteau B, Bohmann D, and Jasper H (2011). Redox regulation by Keap1 and Nrf2 controls intestinal stem cell proliferation in Drosophila. Cell Stem Cell 8, 188–199. [PubMed: 21295275]

Hong Z, Chen KH, DasGupta A, Potus F, Dunham-Snary K, Bonnet S, Tian L, Fu J, Breuils-Bonnet S, Provencher S, et al. (2017). MicroRNA-138 and MicroRNA-25 Down-regulate Mitochondrial Calcium Uniporter, Causing the Pulmonary Arterial Hypertension Cancer Phenotype. Am. J. Respir. Crit. Care Med 195, 515–529. [PubMed: 27648837]

Hu DJ, and Jasper H (2019). Control of Intestinal Cell Fate by Dynamic Mitotic Spindle Repositioning Influences Epithelial Homeostasis and Longevity. Cell Rep. 28, 2807–2823.e2805. [PubMed: 31509744]

Hung YP,Albeck JG, Tantama M, and Yellen G (2011). Imaging cytosolic NADH-NAD(+) redox state with a genetically encoded fluorescent biosensor. Cell Metab. 14, 545–554. [PubMed: 21982714]

Hur JH, Bahadorani S, Graniel J, Koehler CL, Ulgherait M, Rera M, Jones DL, and Walker DW (2013). Increased longevity mediated by yeast NDI1 expression in Drosophila intestinal stem and progenitor cells. Aging (Albany NY) 5, 662–681. [PubMed: 24038661]

Iatsenko I, Boquete JP, and Lemaitre B (2018). Microbiota-Derived Lactate Activates Production of Reactive Oxygen Species by the Intestinal NADPH Oxidase Nox and Shortens Drosophila Lifespan. Immunity 49, 929–942.e5. [PubMed: 30446385]

Jasper H (2020). Intestinal Stem Cell Aging: Origins and Interventions. Annu. Rev. Physiol 82, 203–226. [PubMed: 31610128]

Jiang H, Patel PH, Kohlmaier A, Grenley MO, McEwen DG, and Edgar BA (2009). Cytokine/Jak/Stat signaling mediates regeneration and homeostasis in the Drosophila midgut. Cell 137, 1343–1355. [PubMed: 19563763]

Joseph A-M, Adhihetty PJ, and Leeuwenburgh C (2016). Beneficial effects of exercise on age-related mitochondrial dysfunction and oxidative stress in skeletal muscle. J. Physiol 594, 5105–5123. [PubMed: 26503074]

Kwong JQ, Lu X, Correll RN, Schwanekamp JA, Vagnozzi RJ, Sargent MA, York AJ, Zhang J, Bers DM, and Molkentin JD (2015). The Mitochondrial Calcium Uniporter Selectively Matches Metabolic Output to Acute Contractile Stress in the Heart. Cell Rep. 12, 15–22. [PubMed: 26119742]

Lee T, and Luo L (2001). Mosaic analysis with a repressible cell marker (MARCM) for Drosophila neural development. Trends Neurosci. 24, 251–254. [PubMed: 11311363]

Lee S-M, Dho SH, Ju S-K, Maeng J-S, Kim J-Y, and Kwon K-S (2012). Cytosolic malate dehydrogenase regulates senescence in human fibroblasts. Biogerontology 13, 525–536. [PubMed: 22971926]

Lee KS, Huh S, Lee S, Wu Z, Kim AK, Kang HY, and Lu B (2018). Altered ER-mitochondria contact impacts mitochondria calcium homeostasis and contributes to neurodegeneration in vivo in disease models. Proc. Natl. Acad. Sci. USA 115, E8844–E8853. [PubMed: 30185553]

Li H, Qi Y, and Jasper H (2016). Preventing Age-Related Decline of Gut Compartmentalization Limits Microbiota Dysbiosis and Extends Lifespan. Cell Host Microbe 19, 240–253. [PubMed: 26867182]

Lu J (2019). The Warburg metabolism fuels tumor metastasis. Cancer Metastasis Rev. 38, 157–164. [PubMed: 30997670]

Luongo TS, Lambert JP, Yuan A, Zhang X, Gross P, Song J, Shanmughapriya S, Gao E, Jain M, Houser SR, et al. (2015). The Mitochondrial Calcium Uniporter Matches Energetic Supply with Cardiac Workload during Stress and Modulates Permeability Transition. Cell Rep. 12, 23–34. [PubMed: 26119731]

Marcu R,Wiczer BM, Neeley CK, and Hawkins BJ (2014). Mitochondrial matrix Ca^{2+} accumulation regulates cytosolic NAD^{+}/NADH metabolism, protein acetylation, and sirtuin expression. Mol. Cell. Biol 34, 2890–2902. [PubMed: 24865966]

Mattila J, Kokki K, Hietakangas V, and Boutros M (2018). Stem Cell Intrinsic Hexosamine Metabolism Regulates Intestinal Adaptation to Nutrient Content. Dev. Cell 47, 112–121.e3. [PubMed: 30220570]

McGuire SE, Mao Z, and Davis RL (2004). Spatiotemporal gene expression targeting with the TARGET and gene-switch systems in Drosophila. Sci. STKE 2004, pl6. [PubMed: 14970377]

Miguel-Aliaga I, Jasper H, and Lemaitre B (2018). Anatomy and Physiology of the Digestive Tract of *Drosophila melanogaster*. Genetics 210, 357–396. [PubMed: 30287514]

Ojaimi J, Masters CL, Opeskin K, McKelvie P, and Byrne E (1999). Mitochondrial respiratory chain activity in the human brain as a function of age. Mech. Ageing Dev 111, 39–47. [PubMed: 10576606]

Orr AL, Vargas L,Turk CN, Baaten JE, Matzen JT, Dardov VJ, Attle SJ, Li J, Quackenbush DC, Goncalves RL, et al. (2015). Suppressors of superoxide production from mitochondrial complex III. Nat. Chem. Biol 11, 834–836. [PubMed: 26368590]

Palikaras K, Lionaki E, and Tavernarakis N (2015). Coordination of mitophagy and mitochondrial biogenesis during ageing in C. elegans. Nature 521, 525–528. [PubMed: 25896323]

Parekh AB (2017). Regulation of CRAC channels by Ca^{2+}-dependent inactivation. Cell Calcium 63, 20–23. [PubMed: 28043696]

Paul MK, Bisht B, Darmawan DO, Chiou R, Ha VL, Wallace WD, Chon AT, Hegab AE, Grogan T, Elashoff DA, et al. (2014). Dynamic changes in intracellular ROS levels regulate airway basal stem cell homeostasis through Nrf2-dependent Notch signaling. Cell Stem Cell 15, 199–214. [PubMed: 24953182]

Quinlan CL, Perevoshchikova IV, Hey-Mogensen M, Orr AL, and Brand MD (2013). Sites of reactive oxygen species generation by mitochondria oxidizing different substrates. Redox Biol. 1, 304–312. [PubMed: 24024165]

Rana A, Rera M, and Walker DW (2013). Parkin overexpression during aging reduces proteotoxicity, alters mitochondrial dynamics, and extends lifespan. Proc. Natl. Acad. Sci. USA 110, 8638–8643. [PubMed: 23650379]

Rana A, Oliveira MP, Khamoui AV, Aparicio R, Rera M, Rossiter HB, and Walker DW (2017). Promoting Drp1-mediated mitochondrial fission in midlife prolongs healthy lifespan of Drosophila melanogaster. Nat. Commun 8, 448. [PubMed: 28878259]

Ravera S, Podestà M, Sabatini F, Dagnino M, Cilloni D, Fiorini S, Barla A, and Frassoni F (2019). Discrete Changes in Glucose Metabolism Define Aging. Sci. Rep 9, 10347. [PubMed: 31316102]

Redza-Dutordoir M, and Averill-Bates DA (2016). Activation of apoptosis signalling pathways by reactive oxygen species. Biochim. Biophys. Acta 1863, 2977–2992. [PubMed: 27646922]

Ren T, Zhang H, Wang J, Zhu J, Jin M, Wu Y, Guo X, Ji L, Huang Q, Zhang H, et al. (2017). MCU-dependent mitochondrial Ca^{2+} inhibits NAD^{+}/SIRT3/SOD2 pathway to promote ROS production and metastasis of HCC cells. Oncogene 36, 5897–5909. [PubMed: 28650465]

Rera M, Bahadorani S, Cho J, Koehler CL, Ulgherait M, Hur JH, Ansari WS, Lo T Jr., Jones DL, and Walker DW (2011). Modulation of longevity and tissue homeostasis by the Drosophila PGC-1 homolog. Cell Metab. 14, 623–634. [PubMed: 22055505]

San Martín A, Ceballo S, Ruminot I, Lerchundi R, Frommer WB, and Barros LF (2013). A genetically encoded FRET lactate sensor and its use to detect the Warburg effect in single cancer cells. PLoS One 8, e57712. [PubMed: 23469056]

Santidrian AF, Matsuno-Yagi A, Ritland M, Seo BB, LeBoeuf SE, Gay LJ, Yagi T, and Felding-Habermann B (2013). Mitochondrial complex I activity and NAD+/NADH balance regulate breast cancer progression. J. Clin. Invest 123, 1068–1081. [PubMed: 23426180]

Sanz A, Soikkeli M, Portero-Otín M, Wilson A, Kemppainen E, McIlroy G, Ellilä S, Kemppainen KK, Tuomela T, Lakanmaa M, et al. (2010). Expression of the yeast NADH dehydrogenase Ndi1 in Drosophila confers increased lifespan independently of dietary restriction. Proc. Natl. Acad. Sci. USA 107,9105–9110. [PubMed: 20435911]

Schell JC, Olson KA, Jiang L, Hawkins AJ, Van Vranken JG, Xie J, Egnatchik RA, Earl EG, DeBerardinis RJ, and Rutter J (2014). A role for the mitochondrial pyruvate carrier as a repressor of the Warburg effect and colon cancer cell growth. Mol. Cell 56, 400–413. [PubMed: 25458841]

Schell JC, Wisidagama DR, Bensard C, Zhao H, Wei P, Tanner J, Flores A, Mohlman J, Sorensen LK, Earl CS, et al. (2017). Control of intestinal stem cell function and proliferation by mitochondrial pyruvate metabolism. Nat. Cell Biol 19, 1027–1036. [PubMed: 28812582]

Schieber M, and Chandel NS (2014). ROS function in redox signaling and oxidative stress. Curr. Biol 24, R453–R462. [PubMed: 24845678]

Scialò F, Sriram A, Fernández-Ayala D, Gubina N, Lõhmus M, Nelson G, Logan A, Cooper HM, Navas P, Enríquez JA, et al. (2016). Mitochondrial ROS Produced via Reverse Electron Transport Extend Animal Lifespan. Cell Metab. 23, 725–734. [PubMed: 27076081]

Short KR, Bigelow ML, Kahl J, Singh R, Coenen-Schimke J, Raghavakaimal S, and Nair KS (2005). Decline in skeletal muscle mitochondrial function with aging in humans. Proc. Natl. Acad. Sci. USA 102, 5618–5623. [PubMed: 15800038]

Singh SR, Zeng X, Zhao J, Liu Y, Hou G, Liu H, and Hou SX (2016). The lipolysis pathway sustains normal and transformed stem cells in adult Drosophila. Nature 538, 109–113. [PubMed: 27680705]

Siudeja K, Nassari S, Gervais L, Skorski P, Lameiras S, Stolfa D, Zande M, Bernard V, Frio TR, and Bardin AJ (2015). Frequent Somatic Mutation in Adult Intestinal Stem Cells Drives Neoplasia and Genetic Mosaicism during Aging. Cell Stem Cell 17, 663–674. [PubMed: 26607382]

Srinivas Bharath MM (2017). Post-Translational Oxidative Modifications of Mitochondrial Complex I (NADH: Ubiquinone Oxidoreductase): Implications for Pathogenesis and Therapeutics in Human Diseases. J. Alzheimers Dis 60, S69–S86. [PubMed: 28582861]

Stein LR, and Imai S (2012). The dynamic regulation of NAD metabolism in mitochondria. Trends Endocrinol. Metab 23, 420–428. [PubMed: 22819213]

Stram AR, and Payne RM (2016). Post-translational modifications in mitochondria: protein signaling in the powerhouse. Cell. Mol. Life Sci 73, 4063–4073. [PubMed: 27233499]

Stringer C, Michaelos M, and Pachitariu M (2020). Cellpose: a generalist algorithm for cellular segmentation. bioRxiv, 2020.2002.2002.931238.

Stroud DA, Surgenor EE, Formosa LE, Reljic B, Frazier AE, Dibley MG, Osellame LD, Stait T, Beilharz TH, Thorburn DR, et al. (2016). Accessory subunits are integral for assembly and function of human mitochondrial complex I. Nature 538, 123–126. [PubMed: 27626371]

Tang HW, Liao HM, Peng WH, Lin HR, Chen CH, and Chen GC (2013). Atg9 interacts with dTRAF2/TRAF6 to regulate oxidative stress-induced JNK activation and autophagy induction. Dev. Cell 27, 489–503. [PubMed: 24268699]

Tantama M, Martínez-François JR, Mongeon R, and Yellen G (2013). Imaging energy status in live cells with a fluorescent biosensor of the intracellular ATP-to-ADP ratio. Nat. Commun 4, 2550. [PubMed: 24096541]

Tormos KV, Anso E, Hamanaka RB, Eisenbart J, Joseph J, Kalyanaraman B, and Chandel NS (2011). Mitochondrial complex III ROS regulate adipocyte differentiation. Cell Metab. 14, 537–544. [PubMed: 21982713]

Tosatto A, Sommaggio R, Kummerow C, Bentham RB, Blacker TS, Berecz T, Duchen MR, Rosato A, Bogeski I, Szabadkai G, et al. (2016). The mitochondrial calcium uniporter regulates breast cancer progression via HIF-1α. EMBO Mol. Med 8, 569–585. [PubMed: 27138568]

Triepels R, Smeitink J, Loeffen J, Smeets R, Buskens C,Trijbels F, and van den Heuvel L (1999). The human nuclear-encoded acyl carrier subunit (NDUFAB1) of the mitochondrial complex I in human pathology. J. Inherit. Metab. Dis 22, 163–173. [PubMed: 10234612]

Tufi R, Gleeson TP, von Stockum S, Hewitt VL, Lee JJ, Terriente-Felix A, Sanchez-Martinez A, Ziviani E, and Whitworth AJ (2019). Comprehensive Genetic Characterization of Mitochondrial Ca(2+) Uniporter Components Reveals Their Different Physiological Requirements In Vivo. Cell Rep. 27, 1541–1550.e1545. [PubMed: 31042479]

Urra FA, Muñoz F, Lovy A, and Cárdenas C (2017). The Mitochondrial Complex(I)ty of Cancer. Front. Oncol 7, 118. [PubMed: 28642839]

Vander Heiden MG, and DeBerardinis RJ (2017). Understanding the Intersections between Metabolism and Cancer Biology. Cell 168, 657–669. [PubMed: 28187287]

von Stockum S, Giorgio V, Trevisan E, Lippe G, Glick GD, Forte MA, Da-Rè C, Checchetto V, Mazzotta G, Costa R, et al. (2015). F-ATPase of Drosophila melanogaster forms 53-picosiemen (53-pS) channels responsible for mitochondrial Ca2+-induced Ca2+ release. J. Biol. Chem 290,4537–4544. [PubMed: 25550160]

Wang C, Zhao R, Huang P, Yang F, Quan Z, Xu N, and Xi R (2013). APC loss-induced intestinal tumorigenesis in Drosophila: Roles of Ras in Wnt signaling activation and tumor progression. Dev. Biol 378, 122–140. [PubMed: 23570874]

Wang L, Zeng X, Ryoo HD, and Jasper H (2014). Integration of UPRER and oxidative stress signaling in the control of intestinal stem cell proliferation. PLoS Genet. 10, e1004568. [PubMed: 25166757]

Wu LE, Gomes AP, and Sinclair DA (2014). Geroncogenesis: metabolic changes during aging as a driver of tumorigenesis. Cancer Cell 25, 12–19. [PubMed: 24434207]

Xu C, Luo J, He L, Montell C, and Perrimon N (2017). Oxidative stress induces stem cell proliferation via TRPA1/RyR-mediated Ca^{2+} signaling in the *Drosophila* midgut. eLife 6, e22441. [PubMed: 28561738]

Xu C, Ericsson M, and Perrimon N (2018). Understanding cellular signaling and systems biology with precision: A perspective from ultrastructure and organelle studies in the *Drosophila* midgut. Curr. Opin. Syst. Biol 11, 24–31. [PubMed: 31595264]

Yen TC, Chen YS, King KL, Yeh SH, and Wei YH (1989). Liver mitochondrial respiratory functions decline with age. Biochem. Biophys. Res. Commun 165, 944–1003. [PubMed: 2610701]

Yun J, and Finkel T (2014). Mitohormesis. Cell Metab. 19, 757–766. [PubMed: 24561260]

Zhao Y, Hu Q, Cheng F, Su N, Wang A, Zou Y, Hu H, Chen X, Zhou HM, Huang X, et al. (2015). SoNar, a Highly Responsive NAD+/NADH Sensor, Allows High-Throughput Metabolic Screening of Anti-tumor Agents. Cell Metab. 21, 777–789. [PubMed: 25955212]

Zhao Y, Wang A, Zou Y, Su N, Loscalzo J, and Yang Y (2016). In vivo monitoring of cellular energy metabolism using SoNar, a highly responsive sensor for NAD(+)/NADH redox state. Nat. Protoc 11, 1345–1359. [PubMed: 27362337]

Zhu J, King MS,Yu M, Klipcan L, Leslie AG, and Hirst J (2015). Structure of subcomplex Iβ of mammalian respiratory complex I leads to new super-numerary subunit assignments. Proc. Natl. Acad. Sci. USA 112,12087–12092. [PubMed: 26371297]

Highlights

- Changes in stem cell activity and metabolism are linked by Ca^{2+}
- Rises in mitochondrial Ca^{2+} enhance electron transport chain activity
- Mitochondrial Ca^{2+} declines with age, promoting metabolic reprogramming
- Warburg-like metabolic reprogramming contributes to age-related tissue dysplasia

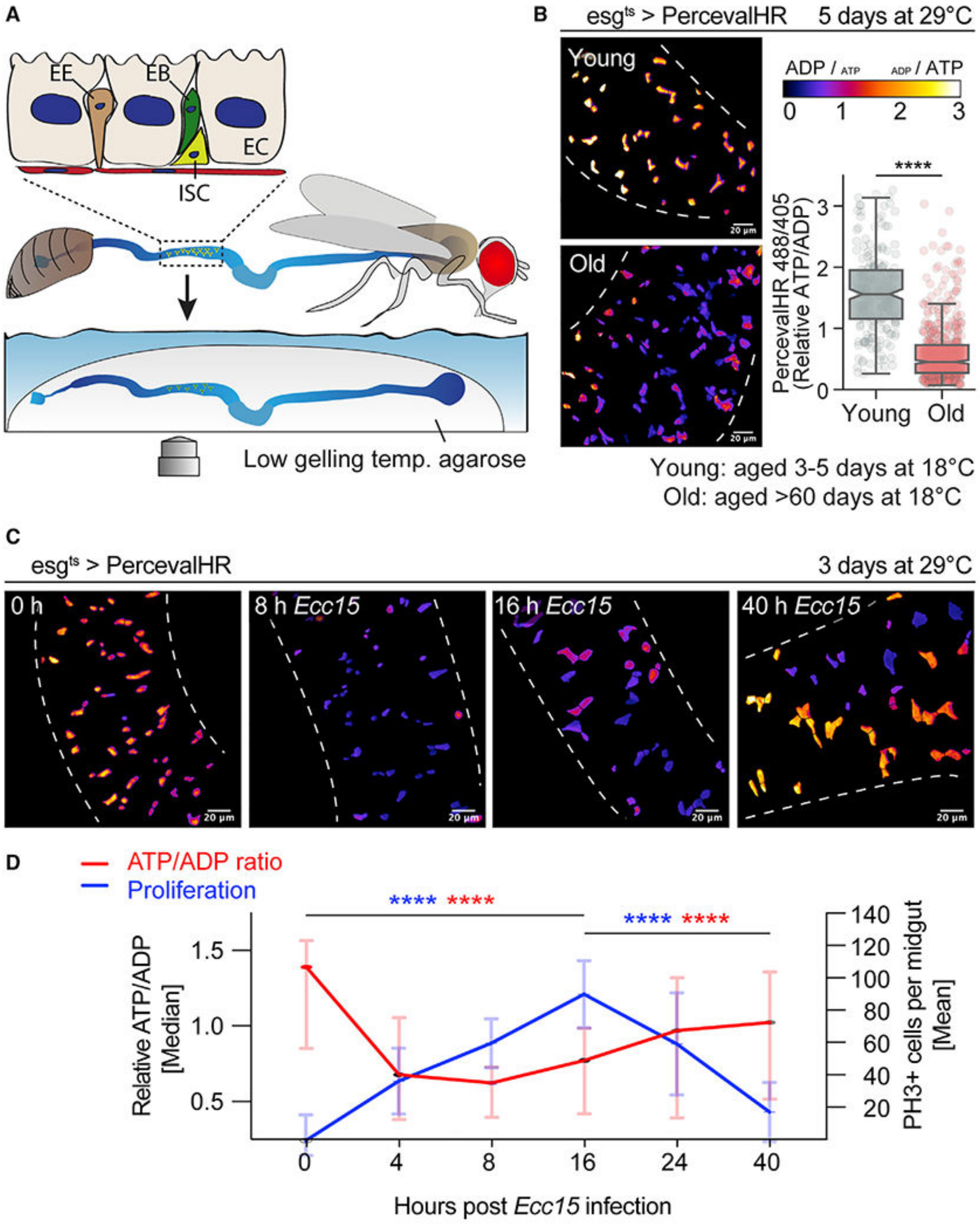

Figure 1. ATP/ADP Ratios Transiently Decrease during the Activation of Young Progenitor Cells but Are Chronically Low in Old Progenitor Cells

(A) Experimental setup for *ex vivo* live-imaging recordings. Labeled cell types: intestinal stem cell (ISC), enteroblast (EB), enterocyte (EC), and enteroendocrine (EE).

(B–D) Representative ratio-images and mean intensity per cell measurements from live imaging of midguts expressing the ratiometric PercevalHR ATP/ADP sensor in ISCs + EBs. Line graphs in (D) present median ± interquartile range ADP/ATP ratios (red) and the mean (SD) number of PH3 positive cells (blue) per midgut recorded at indicated time points post

Ecc15 infection in parallel experiments. Data are presented in separate plots in Figures S1D and S1E.

Boxplots display median ± interquartile range. ****$p < 0.0001$ based on Kruskal-Wallis test with Dunn's multiple comparison tests for ADP/ATP measurements (red stars), and a one-way ANOVA with Holm-Sidak multiple comparison tests for PH3 counts (blue stars). See Table S1 for n values. Dotted lines mark the outline of midguts. Scale bars: 20 μm. See also Figure S1.

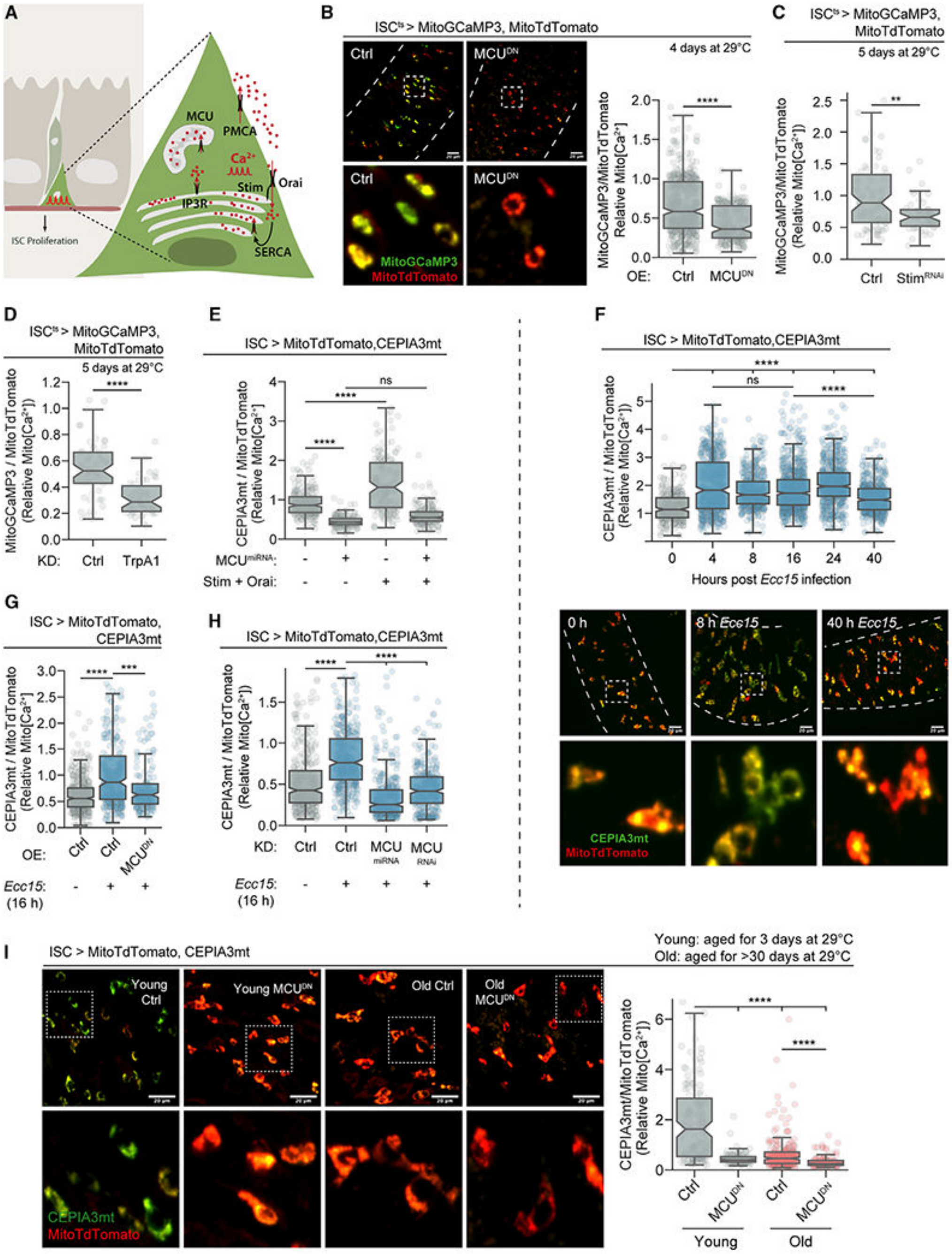

Figure 2. Young ISCs Uptake Ca^{2+} by MCU Complex, whereas Old ISCs Lack Efficient MCU Complex Activity

(A) Scheme illustrating Ca^{2+} pumps, channels, and stores in ISCs. Quiescent ISCs exhibit small, regular Cyto[Ca^{2+}] oscillations, and large, slow Cyto[Ca^{2+}] oscillations drive ISC activation.

(B–I) Representative composite images and/or mean intensity per cell measurements from live imaging of midguts expressing the mitochondrial Ca^{2+} sensors MitoGCaMP3 (B–D) or CEPIA3mt (E–I), in combination with MitoTdTomato in ISCs. MitoGCaMP3/MitoTdTomato or CEPIA3mt/MitoTdTomato fluorescence ratios report relative Mito[Ca^{2+}].

Boxplots display median ± interquartile range. ****$p < 0.0001$; ***$p < 0.001$; **$p < 0.01$; *$p < 0.05$; ns, not significant based on Mann Whitney U test (B–D) or Kruskal-Wallis test with Dunn’s multiple comparison tests (E–I). See Table S1 for n values. OE, overexpression; KD, knockdown. Dotted lines mark the outline of midguts. Dotted squares mark zoomed-in regions. Scale bars: 20 μm. See also Figure S2 and Videos S1, S2, S3, S4, and S5.

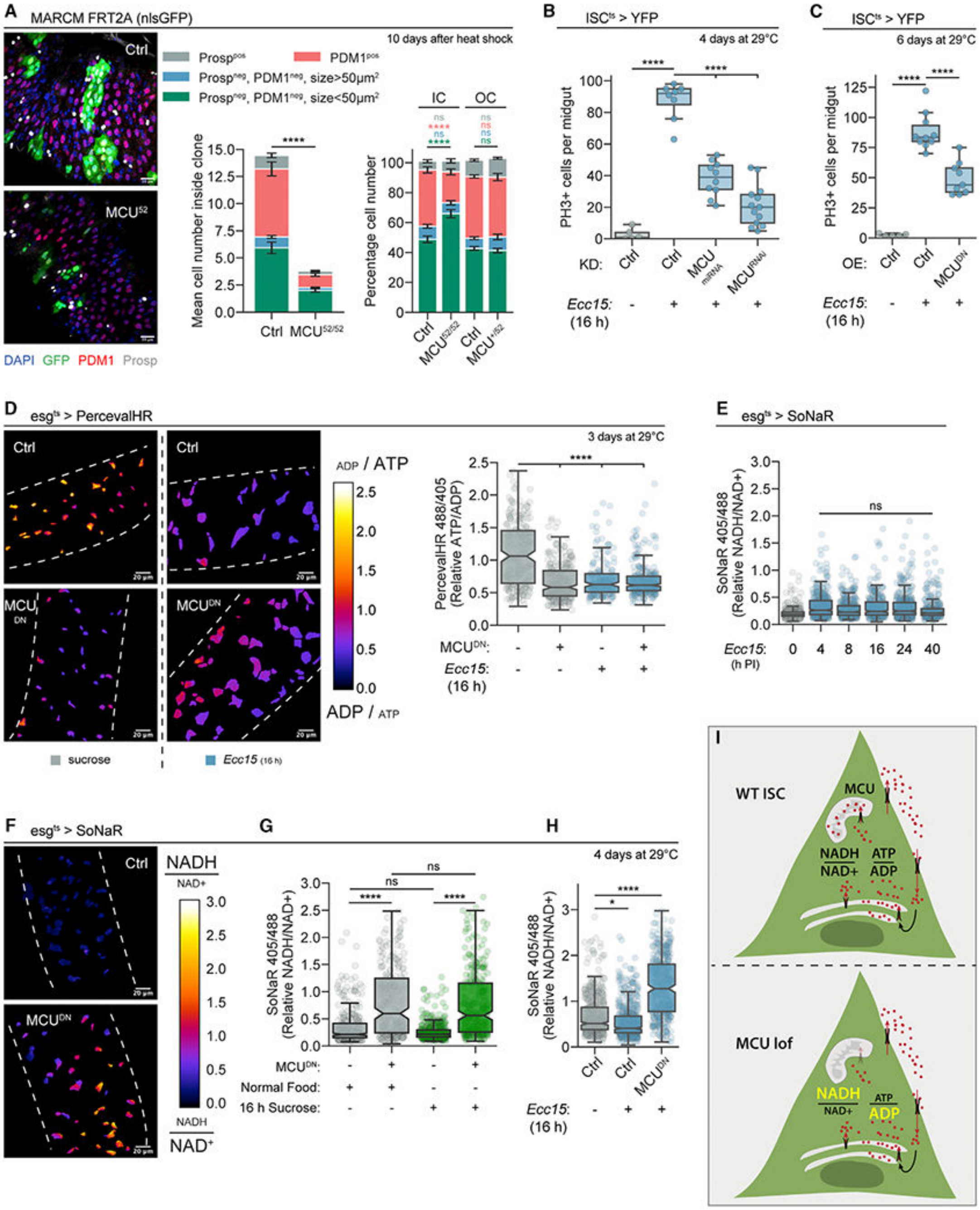

Figure 3. Mito[Ca^{2+}] Supports the Proliferative Activity and Metabolic Homeostasis of Young ISCs

(A) Representative images of MARCM clones 10 days after heat shock. Quantification depicts mean number or percentage ± SEM of each cell type inside each clone (IC) and outside each clone (OC).

(B and C) Number of PH3-positive cells per midgut at time point 16 h post *Ecc15* infection or mock sucrose feeding.

(D) Representative ratio-images and mean intensity per cell measurements from live imaging of midguts expressing the ratiometric PercevalHR ATP/ADP sensor in ISCs + EBs.

(E–H) Representative ratio-images and/or mean intensity per cell measurements from live imaging of midguts expressing the ratiometric PercevalHR ATP/ADP sensor in ISCs + EBs. Sucrose data from (G) are represented as individual channels in Figure S3H.

(I) Scheme depicting altered NADH/NAD+ and ATP/ADP ratios in MCU loss-of-function ISCs.

Boxplots display median ± interquartile range. ****$p < 0.0001$; ***$p < 0.001$; **$p < 0.01$; *$p < 0.05$; ns: not significant based on one-way ANOVA with Holm-Sidak multiple comparison tests (A–C) or Kruskal-Wallis test with Dunn's multiple comparison tests (D–H). See Table S1 for n values. Dotted lines mark the outline of midguts. Scale bars: 20 μm. See also Figure S3.

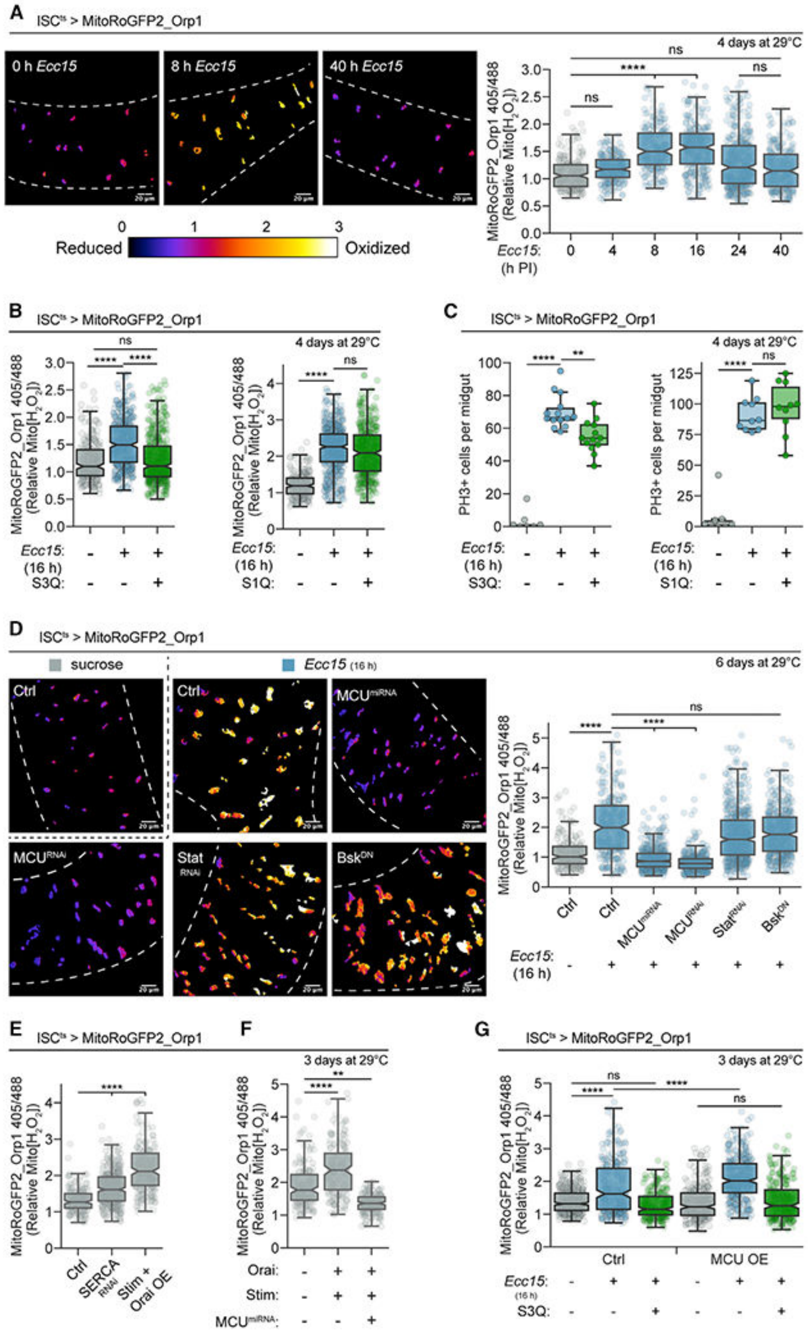

Figure 4. Mito[Ca^{2+}] Increases in Young, Activated ISCs Promote H_2O_2 Generation Downstream of Electron Leak from ETC-CIII

(A, B, and D–G) Representative ratio-images and/or mean intensity per cell measurements from live imaging of midguts expressing the ratiometric MitoRoGFP2_Orp1 sensor in ISCs.

(C) Co-feeding S3QEL2, but not S1QEL1.1, lowers the number of PH3-positive cells per gut 16 h post *Ecc15* infection.

Boxplots display median ± interquartile range. ****$p < 0.0001$; ***$p < 0.001$; **$p < 0.01$; *$p < 0.05$; ns: not significant based on Kruskal-Wallis test with Dunn's multiple comparison tests (A, B, and D–G) or one-way ANOVA with Holm-Sidak multiple comparison tests (C).

See Table S1 for n values. Dotted lines mark the outline of midguts. Scale bars: 20 μm. See also Figure S4.

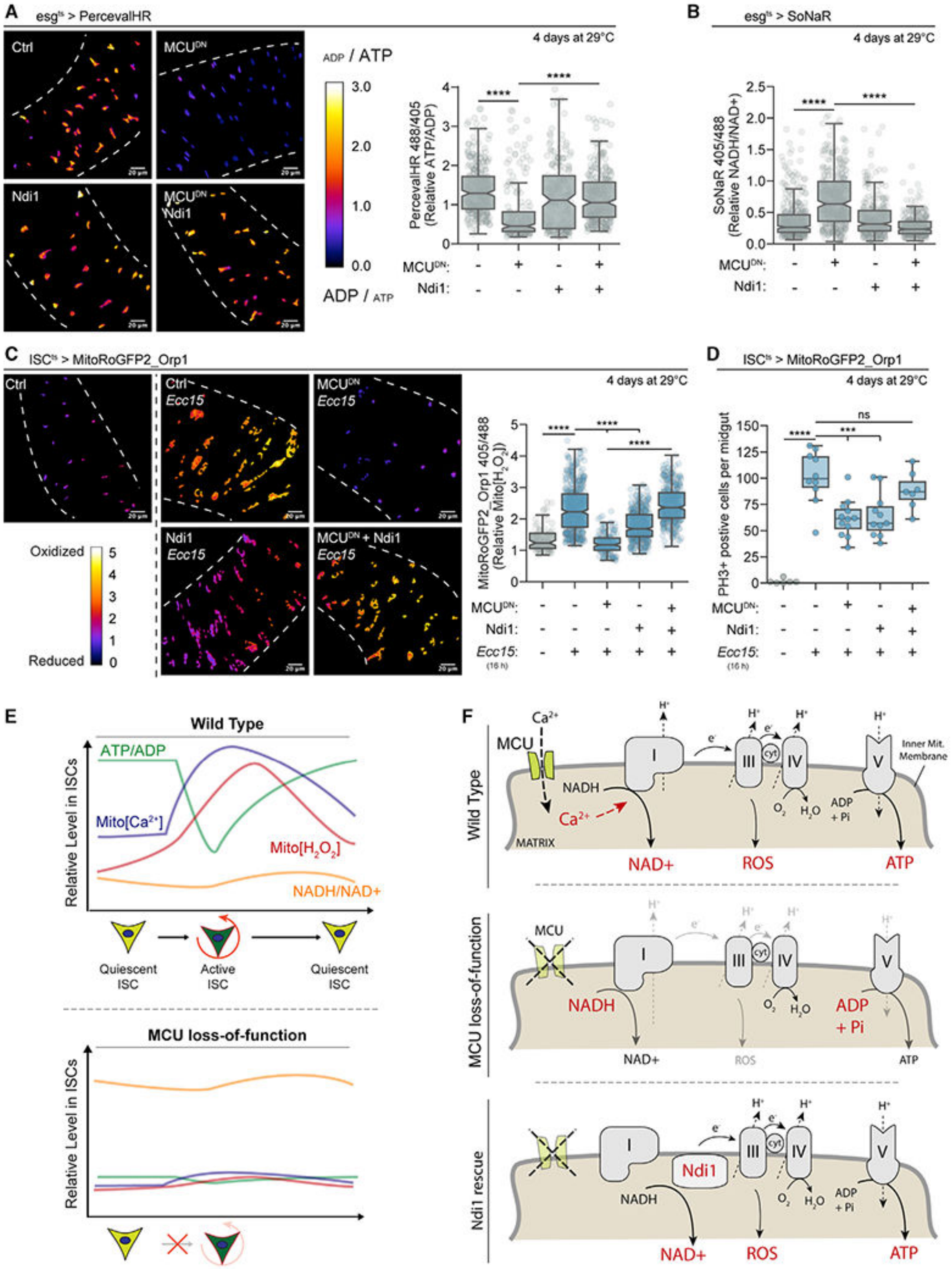

Figure 5. Ndi1 Rescues MCU Loss-of-Function in Young ISCs

(A–C) Representative ratio-images and/or mean intensity per cell measurements from live imaging of midguts expressing the ratiometric PercevalHR (A), SoNaR (B), or MitoRoGFP2_Orp1 (C) sensors in ISCs + EBs (A and B) or ISCs only (C).

(D) Co-expression of Ndi1 rescues proliferative activity of ISCs harboring MCU loss-of-function. Number of PH3-positive cells per midgut at time point 16 h post *Ecc15* infection or mock sucrose feeding.

(E) Model summarizing the coordinated changes in Mito[Ca^{2+}], ATP/ADP, NADH/NAD+, and Mito[H_2O_2] that accompany ISC activation during regenerative episodes (top panel), as well as the altered metabolism of ISCs lacking MCU activity (bottom panel).

(F) Schemes illustrating the regulation of ETC activity by Mito[Ca^{2+}] in ISCs (top panel), impact of MCU loss-of-function upon ETC activity (middle panel), and the putative mechanism by which Ndi1 expression rescues MCU loss-of-function (bottom panel).

Boxplots display median ± interquartile range. ****$p < 0.0001$; ***$p < 0.001$; **$p < 0.01$; *$p < 0.05$; ns: not significant based on Kruskal-Wallis test with Dunn's multiple comparison tests (A–C) or one-way ANOVA with Holm-Sidak multiple comparison tests (D). See Table S1 for n values. Dotted lines mark the outline of midguts. Scale bars: 20 μm. See also Figure S5.

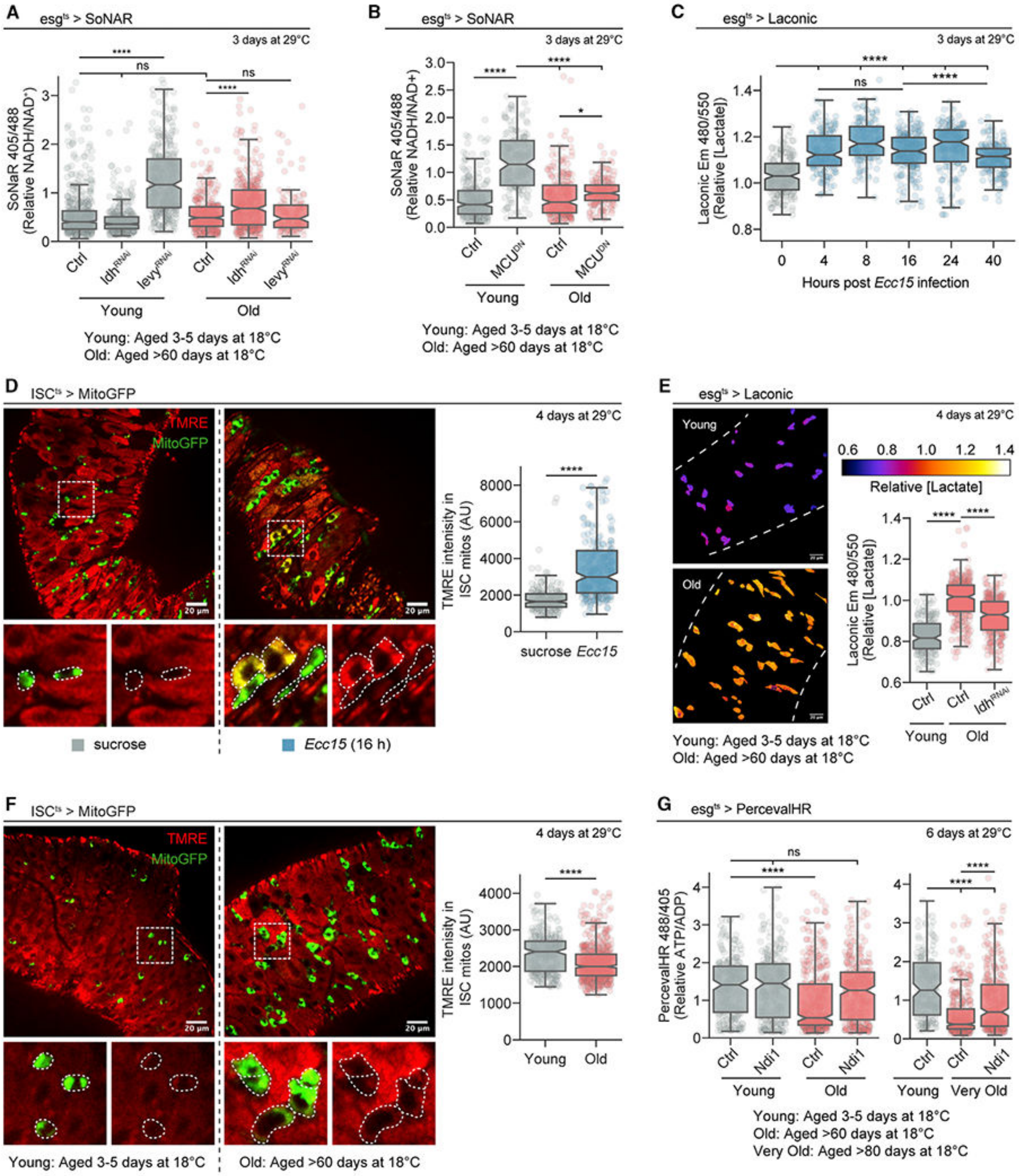

Figure 6. Deficient Mito Ca^{2+} Uptake Contributes to a "Warburg-like" Metabolic Switch in Old ISCs

(A–C, E, and G) Representative ratio-images and/or mean intensity per cell measurements from live imaging of midguts expressing the ratiometric SoNaR (A and B), Laconic (C and E) or PercevalHR (G) sensors in ISCs + EBs.

(D and F) representative composite images and mean intensity per cell measurements from live imaging of midguts expressing MitoGFP in ISCs and incubated with the potentiometric dye TMRE. TMRE signal was measured in ISC mitochondria, as outlined by MitoGFP.

Dotted squares mark zoomed-in regions. Within zoomed-in regions, individual cells are circled with a dotted line. AU, arbitrary units.

Boxplots display median ± interquartile range. ****$p < 0.0001$; ***$p < 0.001$; **$p < 0.01$; *$p < 0.05$; ns: not significant based on Kruskal-Wallis test with Dunn’s multiple comparison tests (A–C and G) or Mann-Whitney U test (D–F). See Table S1 for n values. Dotted lines mark the outline of midguts. Scale bars: 20 μm. See also Figure S6.

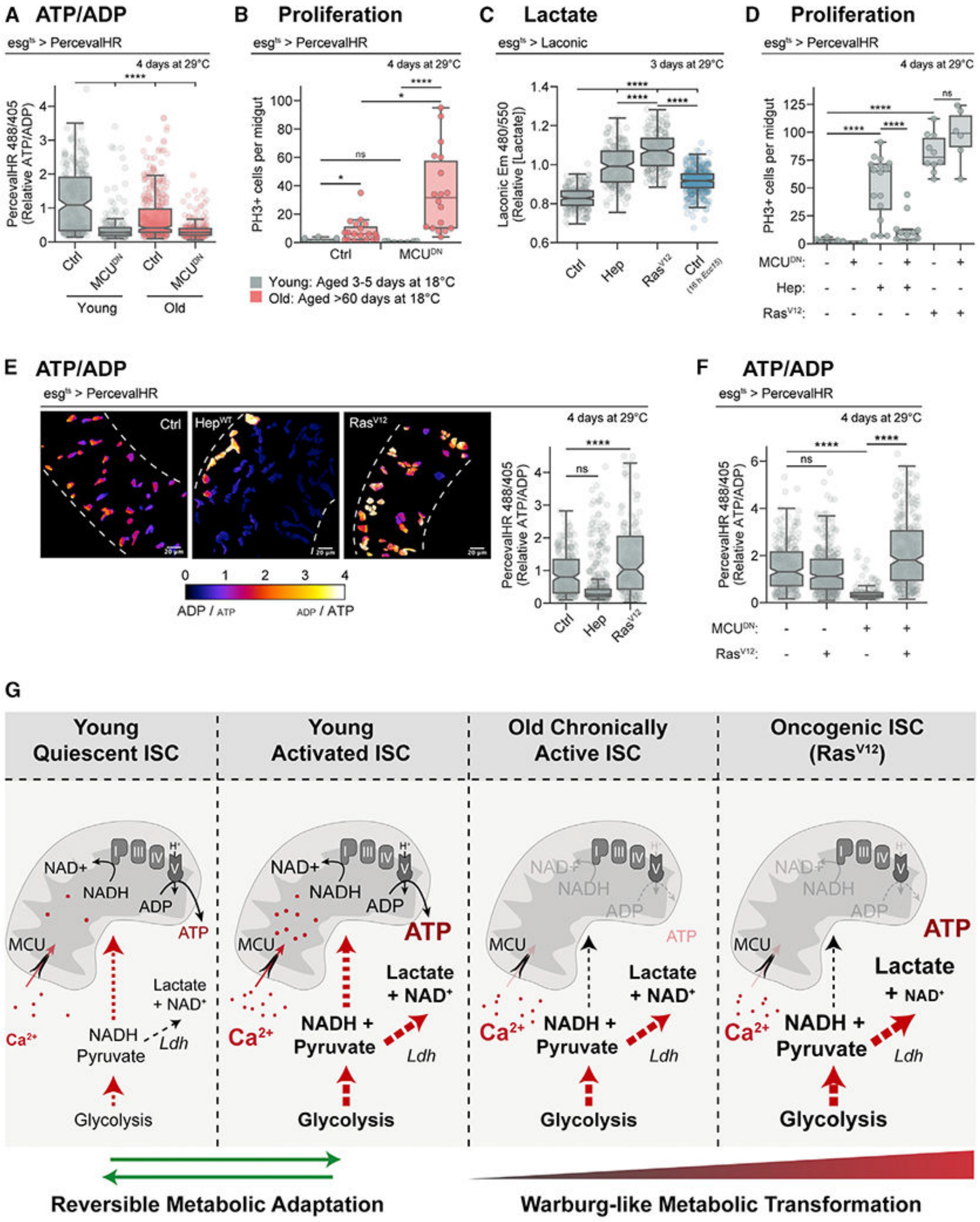

Figure 7. Old ISCs Resemble ISCs Transformed by Oncogenes but Are Not Fully Metabolically Transformed

(A, C, E, and F) Representative ratio-images and/or mean intensity per cell measurements from live imaging of midguts expressing the ratiometric PercevalHR (A, E, and F) or Laconic (C) sensors in ISCs + EBs.

(B and D) The number of PH3-positive cells per midgut.

(G) Scheme depicting metabolic profiles of young, quiescent; young, active; and old chronically active and oncogenic ISCs.

Boxplots display median ± interquartile range. ****$p < 0.0001$; ***$p < 0.001$; **$p < 0.01$; *$p < 0.05$; ns: not significant based on Kruskal-Wallis test with Dunn's multiple comparison tests (A, C, E, and F) or one-way ANOVA with Holm-Sidak multiple comparison tests (B and D). Dotted lines mark the outline of midguts. See Table S1 for n values. Scale bars: 20 μm. See also Figure S7.

KEY RESOURCES TABLE

REAGENT or RESOURCE	**SOURCE**	**IDENTIFIER**
Antibodies		
Mouse anti-prospero	DSHB	Cat#MR1A; RRID: AB_528440
Rabbit anti-phospho-histone H3	EMD Millipore	Cat#06-570; RRID: AB_310177
Rabbit anti-PDM1	Laboratory of Xiaohang Yang at Zhejiang University	N/A
Mouse anti-delta	DSHB	DSHB C594.9B; RRID: AB_528194
Chemicals, Peptides, and Recombinant Proteins		
TMRE	ThermoFisher	Cat # 669
Ionomycin	ThermoFisher	Cat # 1136609
Thapsigardin	Tocris	Cat # 1138
S3QEL2	Tocris	Cat # 5735
S1QEL1.1	Cayman Chemical	Cat # 20982
Experimental Models: Organisms/Strains		
Drosophila melanogaster UAS::MitoRoGFP2_Orp1	BDSC	Cat # 67667
Drosophila melanogaster UAS::MitoRoGFP2_Grx1	BDSC	Cat # 67664
Drosophila melanogaster UAS::SERCA^{RNAi}	BDSC	Cat # 44581
Drosophila melanogaster UAS::Stim^{RNAi}	BDSC	Cat # 27263
Drosophila melanogaster UAS::TrpA1^{RNAi}	BDSC	Cat # 31504
Drosophila melanogaster UAS::Ras^{V12}	BDSC	Cat # 64196
Drosophila melanogaster Tub::G80ts	BDSC	Cat # 7017
Drosophila melanogaster Tub::G80ts	BDSC	Cat # 7108
Drosophila melanogaster UAS::MitoGFP	BDSC	Cat # 84977
Drosophila melanogaster UAS::GCaMP3	BDSC	Cat # 32235
Drosophila melanogaster UAS::mCherry	BDSC	Cat # 52267
Drosophila melanogaster UAS::MCU^{RNAi}	VDRC	Cat # 110781
Drosophila melanogaster UAS::Stat^{RNAi}	VDRC	Cat # 106980
Drosophila melanogaster UAS::levy^{RNAi}	VDRC	Cat # 101523
Drosophila melanogaster UAS::PDH-E1a^{RNAi}	VDRC	Cat # 107209
Drosophila melanogaster UAS::MPC1^{RNAi}	VDRC	Cat # 15858
Drosophila melanogaster UAS::Ldh^{RNAi}	VDRC	Cat # 31192
Drosophila melanogaster UAS:Mdh1^{RNAi}	VDRC	Cat # 110604
Drosophila melanogaster UAS::MitoTdTomato	DGRC	Cat #117016
Drosophila melanogaster UAS::LacZ^{RNAi}	Gift from Masayuki Miura at University of Tokyo	N/A
Drosophila melanogaster UAS::MCU^{DN}	Gift from Ronald Davies at The Institute Florida	N/A
Drosophila melanogaster UAS::MCU	Gift from Jongkyeong Chung of Seoul National University	N/A

REAGENT or RESOURCE	SOURCE	IDENTIFIER
Drosophila melanogaster UAS::hMCU	Gift from Jongkyeong Chung of Seoul National University	N/A
Drosophila melanogaster MCU^{52}	Gift from Jongkyeong Chung of Seoul National University	N/A
Drosophila melanogaster UAS::MitoGCaMP3	Gift from Fumiko Kawasaki of Pennsylvania State University	N/A
Drosophila melanogaster UAS::Stim	Gift from Tata Institute of Fundamental Research	N/A
Drosophila melanogaster UAS::Orai	Gift from Tata Institute of Fundamental Research	N/A
Drosophila melanogaster UAS::Bsk^{DN}	Gift from Marek Mlodzik of Icahn School of Medicine	N/A
Drosophila melanogaster UAS::Hep	Gift from Marek Mlodzik of Icahn School of Medicine	N/A
Drosophila melanogaster Su(H)GBE::G80	Gift from Steven Hou of National Cancer Institute	N/A
Drosophila melanogaster UAS::Ndi1	Gift from Howard T. Jacobs of University of Tampere	N/A
Drosophila melanogaster UAS::AOX	Gift from Howard T. Jacobs of University of Tampere	N/A
Drosophila melanogaster UAS::PercevalHR	This paper	N/A
Drosophila melanogaster UAS::SoNaR	This paper	N/A
Drosophila melanogaster UAS::cpYFP	This paper	N/A
Drosophila melanogaster UAS::Mito-R-GECO1	This paper	N/A
Drosophila melanogaster UAS::CEPIA3mt	This paper	N/A
*Drosophila melanogaster UAS::*MCU^{miRNA}	This paper	N/A
Software and Algorithms		
python	conda	3.7
pandas	conda	1.0.3
matplotlib	conda	3.3.1
seaborn	conda	0.10.1
pystackreg	pypi	0.2.2
trackpy	pypi	0.4.2
scikit-image	conda	0.17.2
scikit-learn	conda	0.23.2
scikit-posthocs	pypi	0.6.2
scipy	conda	1.5.0
Napari	conda	0.3.4
Cellpose	Stringer et al., 2020	
StarDist	Schmidt et al., 2018, MICCAI, conference	
ImageJ	NIH	
MATLAB	MathWorks	R2017b
Ilastik	Berg et al., 2019	N/A
Trainable WEKA	Arganda-Carreras et al., 2017	

REAGENT or RESOURCE	SOURCE	IDENTIFIER
Image Analyst MKII	Image Analyst Software, Novato, CA	N/A